

24483

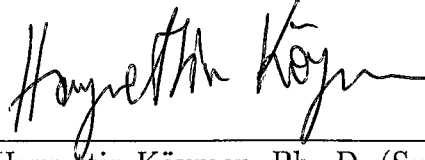
DIGITAL BEAMFORMING TECHNIQUES AND VLSI
CIRCUITS FOR MEDICAL ULTRASOUND IMAGING

A DISSERTATION
SUBMITTED TO THE DEPARTMENT OF ELECTRICAL AND ELECTRONICS
ENGINEERING
AND THE INSTITUTE OF ENGINEERING AND SCIENCE
OF BILKENT UNIVERSITY
IN PARTIAL FULFILLMENT OF THE REQUIREMENTS
FOR THE DEGREE OF
DOCTOR OF PHILOSOPHY

By
Mustafa Karaman
December 1992

T.C. YÜKSEKÖĞRETİM KURULU
DOKÜMANTASYON MERKEZİ

I certify that I have read this thesis and that in my opinion it is fully adequate, in scope and in quality, as a dissertation for the degree of Doctor of Philosophy.



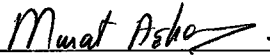
Hayrettin Köymen, Ph. D. (Supervisor)

I certify that I have read this thesis and that in my opinion it is fully adequate, in scope and in quality, as a dissertation for the degree of Doctor of Philosophy.



Abdullah Atalar, Ph. D. (Supervisor)

I certify that I have read this thesis and that in my opinion it is fully adequate, in scope and in quality, as a dissertation for the degree of Doctor of Philosophy.



Murat Aşkar, Ph. D.

I certify that I have read this thesis and that in my opinion it is fully adequate, in scope and in quality, as a dissertation for the degree of Doctor of Philosophy.



Levent Onural, Ph. D.

I certify that I have read this thesis and that in my opinion it is fully adequate, in scope and in quality, as a dissertation for the degree of Doctor of Philosophy.



Mehmet Ali Tan, Ph. D.

I certify that I have read this thesis and that in my opinion it is fully adequate, in scope and in quality, as a dissertation for the degree of Doctor of Philosophy.



Cevdet Aykanat, Ph. D.

Approved for the Institute of Engineering and Science:



Mehmet Baray, Ph. D.

Director of Institute of Engineering and Science

Abstract

DIGITAL BEAMFORMING TECHNIQUES AND VLSI CIRCUITS FOR MEDICAL ULTRASOUND IMAGING

Mustafa Karaman

Ph. D. in Electrical and Electronics Engineering

Supervisors:

Hayrettin Köymen, Ph. D. and Abdullah Atalar, Ph. D.

December 1992

For phased array medical ultrasound imaging, digital beamforming techniques and VLSI circuits are studied to form a fully digital receive front-end hardware. To increase the timing accuracy in beamforming, a computationally efficient upsampling scheme is examined. A digital beamforming method based on receive focusing at the raster focal points is proposed. The sector images of the resolution phantom, reconstructed from the phased array experimental data by beamforming at the radial and raster focal points, are presented for comparison of the image resolution performance of the two beamforming schemes. For adaptive beamforming, a phase aberration correction technique with very low computational complexity is described. Image quality performance of the technique is examined by digitally processing the non-aberrated and aberrated phased array experimental data sets of an ultrasound resolution phantom. VLSI circuits and their implementations for the proposed techniques are presented.

Keywords: Medical ultrasound imaging, digital beamforming, phased array beamforming, phase aberration correction, VLSI circuit.

Özet

TIBBİ ULTRASONİK GÖRÜNTÜLEME İÇİN SAYISAL DEMETLEME YÖNTEMLERİ VE TÜMDEVRELER

Mustafa Karaman

Elektrik ve Elektronik Muhendisligi Doktora

Tez Yöneticileri:

Prof. Dr. Hayrettin Köymen ve Prof. Dr. Abdullah Atalar

Aralık 1992

Evreli dizilerle gerçekleştirilen tıbbi ultrasonik görüntüleme, sayısal bir ön elektronik donanım oluşturmak için sayısal demetleme yöntemleri ve tümleşik devreler önerilmiştir. Zamanlama doğruluğunu arttırmak için verimli bir örnekleme arttırma yöntemi incelenmiştir. Raster noktalara odaklamaya dayalı bir sayısal demetleme yöntemi sunulmuştur. Raster ve radyal noktalara odaklanarak gerçekleştirilen demetleme yöntemlerini karşılaştırmak için, bir ultrasonik fantomdan elde edilen deneysel veriler kullanılarak oluşturulan ultrasonik sektör görüntüleri sunulmuştur. Evre bozukluklarını gerçek zamanda düzeltmek için verimli bir yöntem önerilmiştir. Yöntemin verimliliği, fantomdan deneysel olarak alınan normal ve bozuk evreli veriler kullanılarak incelenmiştir. Önerilen bütün yöntemler için tümdevre yapıları ve bunların yüksek ölçekli tümdevre tasarım teknikleri ile gerçekleştirilmesi sunulmuştur.

Anahtar

sözcükler: Tıbbi ultrasonik görüntüleme, sayısal demetleme, evreli dizilerle demetleme, evre bozukluklarının düzeltilmesi, tümdevre.

Acknowledgement

I would like to express my deepest gratitude to Prof. Dr. Hayrettin Köymen and Prof. Dr. Abdullah Atalar for their supervision, encouragement, and invaluable advice in all steps of the development of this work. It is my extraordinary chance to work with them throughout my graduate study, to be instructed and trained in all aspects of the research.

I would like to thank to Prof. Dr. Matthew O'Donnell of Michigan University for his collaboration. He kindly provided the ultrasound phase array experimental data sets of the phantom, advised in processing of the data, and given valuable commands and revisions on the phase aberration correction part of this work.

I would like to acknowledge the cooperations of Cengiz Aydın, A. Ertuğrul Kolağasıoğlu, M. Şenol Toygar, İ. Adil Baktır, Radwan Tahboub, Engin Erzin, Fırat Kılıç, and M. Hakan Asyalı, in VLSI implementation of the beamformer chip through a VLSI course project.

I would like to thank to Prof. Dr. Murat Aşkar of Middle East Technical University (METU), for his collaboration through NATO SFS Project (TV-Microdesign) and VLSI Design Center of Turkish Scientific and Research Council (TÜBİTAK) in METU. The data files of layout design rules and simulation parameters for CMOS technology of IMEC-MIETEC of Belgium were provided by this project. He was a member of my Ph. D. proposal jury, and offered his motivating and directive commands on my research. I would like to acknowledge the cooperations of his graduate students and research staff in the VLSI Design Center, in particular İ. Enis Urgan and İlhami H. Torunoğlu, in installation of the layout technology files.

I appreciate Assoc. Prof. Dr. Cevdet Aykanat of CEIS Department, a member of my Ph. D. proposal jury, for his valuable discussions on the development of hardware architectures, and for his motivating advises on my research. I would like to thank to Assoc. Prof. Dr. Levent Onural and Assoc. Prof. Dr. Mehmet Ali Tan, the members of my Ph. D. proposal jury, for their motivating and directive commands on my research.

I am grateful to F. Levent Değertekin and Satılmış Topcu for their continuous encouragements in all stages of this study, to Gözde Bozdağı and M. Ogan Ocalı for their helps in producing the photographs of ultrasound images, and to Mürüvvet Parlakay, secretary of EEE Department, for her logistical support, and to all members of EEE Department for their contributions in one way or the other through formal and informal discussions.

I like to acknowledge the financial supports of TÜBİTAK through Acoustic Imaging (Eureka 525) Project and Programme of Support for International Meetings, and the financial support of IEEE Turkey Section, for presentation of this work in the national and international conferences.

Finally, my sincere thanks are due to my family for their continuous moral support throughout my graduate study.

Contents

Abstract	i
Özet	ii
Acknowledgement	iii
Contents	v
List of Figures	vii
List of Tables	x
1 Introduction	1
2 Basics of Ultrasound Imaging	5
2.1 Phased Array Beamforming	6
2.2 B-Mode Sector Imaging	8
2.3 Ultrasound Image Resolution	10
3 Digital Beamforming	11
3.1 Front-End Architecture	11
3.2 Reduction of Delay Quantization Error	12
3.2.1 Interpolation Scheme	13
3.2.2 Hardware Structure for Interpolator	14
3.3 Beamforming at Raster Focal Points	14

3.3.1	Performance Analysis	17
3.3.2	Hardware Structure for Digital Beamformer	25
3.4	Concluding Remarks	27
4	Phase Aberration Correction	29
4.1	Introduction	29
4.2	Technique	32
4.2.1	Approach	32
4.2.2	Averaging of Phase Estimates	33
4.2.3	Reduction of Wordlength	37
4.2.4	Performance Analysis	38
4.3	VLSI Architectures for Phase Estimation	48
4.3.1	Fullword SAD	48
4.3.2	One Bit SAD	48
4.4	Concluding Remarks	52
5	VLSI Circuits	53
5.1	Implementation	53
5.2	Interpolator	54
5.3	Beamformer	55
5.4	Phase Estimator	56
5.5	Concluding Remarks	59
6	Results and Conclusions	60
	Appendix A	65
	Appendix B	68
	Appendix C	70
	Appendix D	75
	Vita	90

List of Figures

1.1	Block diagram of a ultrasound imaging system.	2
2.1	Symbolic representations of analog and digital receive beamforming schemes.	7
2.2	Scanning techniques in ultrasound imaging.	8
2.3	Phased array sector scanning.	9
3.1	Digital receive front-end architecture.	12
3.2	Hardware structure of the linear interpolator.	15
3.3	Radial and raster focal points.	16
3.4	Geometrical configuration for the simulation parameters.	18
3.5	Normalized PSF magnitude. The PSF's in the first and second rows are obtained by beamforming at radial and raster focal points, respectively. The PSF at the first, second and third columns correspond to the point reflectors located at $2D$, $4D$, and $6D$ away from the array, respectively.	19
3.6	Received experimental RF wavefronts across the array. The vertical and horizontal widths of each row correspond to the aperture size and time interval of 512 samples, respectively. The first, second, third and fourth rows show the samples between 1-512, 513-1024, 1025-1536, 1537-2048, respectively.	20
3.7	Digital processing steps for beamforming at radial and raster points.	21
3.8	Interpolation scheme used in the scan-conversion.	23

3.9	Ultrasound sector images of the standard graphite-gel AIUM resolution phantom. The top and bottom images are reconstructed by receive beamforming at radial and raster points, respectively, through the digital processing steps depicted in Fig. 3.7.	24
3.10	Architecture of the beamformer.	26
3.11	Functional structure of the processing unit.	27
4.1	Symbolic representation of the phase aberration in receive beamforming.	30
4.2	Effect of the phase aberration on PSF.	31
4.3	SAD and cross correlation of two sampled RF signals.	33
4.4	Window configuration used for two dimensional SAD minimization.	34
4.5	Control, aberrated and corrected PSF's.	36
4.6	One bit representation of the RF signal.	37
4.7	Received RF wavefronts across the array for the control and aberrated RF data sets. The first, second and third rows show the portions of data sets associated with Plate 0, Plate 1, and Plate 2, respectively. The vertical and horizontal widths of each row correspond to the aperture size and time interval of 512 samples.	39
4.8	Phase aberration patterns of the plates.	40
4.9	Convergence and accuracy performance of phase correction schemes for Plate 0.	41
4.10	Convergence and accuracy performance of phase correction schemes for Plate 1.	42
4.11	Convergence and accuracy performance of phase correction schemes for Plate 2.	43
4.12	Effect of window size on the accuracy of phase estimation techniques for Plate 1.	44
4.13	Effect of the number of scan angles used for the averaging of phase estimates on the accuracy performance the SAD with full word and one bit word length.	45

4.14	Images of a section of the phantom. Control and aberrated images (row 1). The corrected images using full word cross correlation (row 2), full word SAD with weighted average of phase estimates over five scan angles (row 3), and SAD with one bit word length and average of phase estimates over five scan angles (row 4). The images in the first, second and third columns correspond to the data sets associated with Plate 0, Plate 1, and Plate 2, respectively.	46
4.15	Amplitude distortions of the plates across the array.	47
4.16	Full word SAD architecture.	49
4.17	Processing unit for the 1-bit SAD architecture.	50
4.18	The high throughput architecture for 1-bit SAD.	51
5.1	Layout of the designed interpolator chip.	54
5.2	Layout of the designed beamformer chip.	55
5.3	Connections of the beamformer chips for 256 and 128 channels.	56
5.4	Layout of the designed 1-bit SAD chip.	57
5.5	Pipelined data flow scheme of the 1-bit SAD chip.	58
B.1	Numerical simulation results showing the mean and standard deviation of time delay estimate using cross correlation and SAD.	69
C.1	Spatial covariance across the array using correlation (COR) and sum of absolute difference (SAD) for non-focused and focused cases.	72
C.2	Spatial covariance across the array using correlation (COR) and sum of absolute difference (SAD) for non-aberrated and aberrated data.	73
C.3	Spatial covariance across the array using fullword SAD and one-bit SAD.	74
D.1	Beamforming scheme employing parallel phase delay adjustment in subbands of RF signals.	76
D.2	RF Subbands.	77

List of Tables

2.1	Sound parameters in different tissues.	6
3.1	Powers of 2 for T_1 and $8 - T_1$	14
3.2	PSF beamwidths normalized by the ultrasound wavelength. FWHM beamwidth corresponds to -6 dB beamwidth.	19
4.1	RMS error between the estimated and actual aberration patterns (unit: fraction of a wavelength).	35
5.1	Characteristic parameters of the designed chips.	58

Chapter 1

Introduction

Phased-array ultrasound imaging techniques have been extensively used in modern medicine for diagnostic purposes. In reconstruction of phased array ultrasound images, short bursts of ultrasound are transmitted, and echoes reflected from internal structures of body are received by a phased array transducer. The planar cross-section which is to be imaged is scanned by electronically steering and focusing the array both in transmit and receive modes [1, 2, 3, 4]. The signal processing involved in focusing and steering is called as the *beamforming* [5, 6].

Much of the recent increase in use of diagnostic ultrasonic imaging depends on improvements in image quality. New digital imaging systems coming into use hold the promise to further enhance the image quality. The flexibility inherent in digital imaging systems enables the designers to use a wide range of algorithms to reconstruct, enhance, and analyze ultrasonic images [7, 8, 9, 10, 11, 12]. Critical to any digital ultrasonic imaging system is the front-end hardware consisting of transmit and receive beamforming electronics (Fig 1.1). Although imaging capabilities can be augmented by digital processing techniques, the front-end hardware often sets the system performance limits.

Real-time phased array ultrasound beamforming involves significant amount of electronic signal processing at video rates. Transmit beamforming is performed at every scan angle whereas receive beamforming is dynamically repeated for

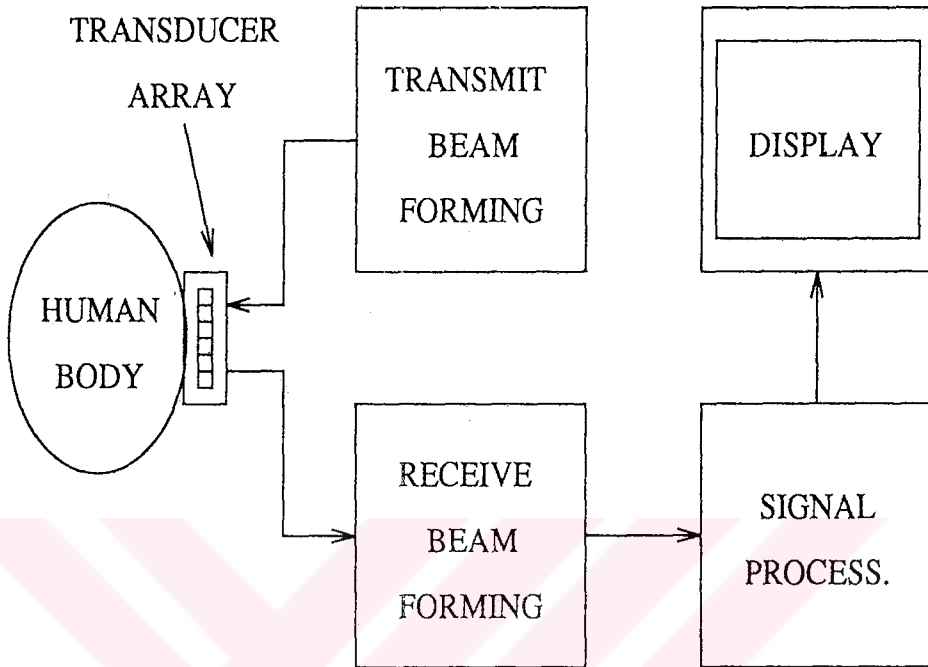


Figure 1.1: Block diagram of a ultrasound imaging system.

every image point. Design of the transmit beamforming electronics is relatively easy, since each array element can be fired by simple timing circuitry, while design of the receive beamforming circuitry is an involved task and have been subject of considerable research [13, 14, 15] Analog receive beamforming hardware is bulky and expensive [16, 17]. Recent developments in digital integrated circuit technology motivates research on advanced digital beamforming techniques based on special purpose VLSI circuits [14]. In design of such circuits, care must be given to the beamforming algorithm performance which critically affects image resolution [18], and on the feasibility of algorithm for VLSI implementation [19]. In this study, we consider three major problems in beamforming: delay quantization, receive focusing used for image reconstruction, and phase aberration. We propose new digital beamforming schemes, and present VLSI circuits for their realizations.

Delay quantization has a significant undesired effect on the transmit and receive responses of the system, which results in an increase in the side lobe

levels of the array response [20, 21, 22, 23]. Accuracy of timing information used in beamforming can be increased using fast analog to digital converters (ADC), with relatively high cost. It can be also solved by employing digital upsampling techniques. Since the timing accuracy in beamforming is much more critical than the amplitude accuracy, as a cost-effective solution for high timing accuracy in beamforming, a linear interpolation scheme with coefficients in discrete powers-of-two space [24] is examined.

In conventional ultrasound imaging, receive beamforming is carried out at the radial focal points. The radial data is converted to the raster data which correspond to the display pixels in rectangular coordinates. The conversion process, called *scan conversion* [6, 25], imposes a significant hardware overhead and may degrade the image quality. To eliminate the scan conversion, an alternative digital beamforming scheme based on receive focusing at the raster points is proposed.

Computation of the timing information required for the beamforming is based on the assumption that the image plane is composed of the uniform soft tissue. This assumption, however, is not valid in general, and causes significant phase errors [26, 27], and hence degradation in image resolution. The solution of this problem involves phase error correction using an adaptive beamforming technique. The algorithm used for this purpose must be computationally efficient for real-time applications. As a solution to this problem, we study a phase aberration correction technique with very low computational complexity, based on the time delay estimation via minimization of the sum of absolute differences between the samples of radio frequency (RF) echo signals of adjacent array elements.

For the interpolation, beamforming, and phase aberration estimation, we also propose the digital hardware architectures and present their implementations using full-custom CMOS VLSI design techniques.

Organization of this dissertation is as follows. In the next chapter, fundamentals of ultrasound imaging are briefly reviewed. Chapter 3 covers the front-end hardware architecture, reduction of delay quantization errors, and

beamforming at raster focal points with the performance analysis. Hardware structures for the interpolator and digital beamformer are also presented. Phase aberration problem is studied in Chapter 4. The proposed phase correction techniques and the performance analysis are presented. Chapter 4 also includes description of the VLSI architectures for phase estimation. VLSI implementation of the interpolator, digital beamformer, and phase estimator are presented in Chapter 5. Finally, the results, conclusions, and further studies are outlined in Chapter 6.



Chapter 2

Basics of Ultrasound Imaging

Main purpose of medical imaging is to observe the internal structures of the body noninvasively. Medical imaging methods are based on the illumination of the tissue by some form of radiation, and reconstruction of the image from the received radiation energy caused by interaction of the transmitted energy with the tissue by means of reflection, absorption, or scattering. In medical imaging applications, various forms of radiation, such as some nuclear particles, X-rays, electric fields, and ultrasound waves have been used for many years. In general, each form of radiation results in imaging of different characteristics of tissue.

Ultrasound is a term used for sound which have frequency above the range of human hearing. Ultrasound waves are used for representation of the *mechanical* properties of tissue (such as density and elasticity). This feature of the ultrasound waves makes ultrasound imaging complementary to other diagnostic tools [2, 28]. On the other hand, the clinical examinations have shown that ultrasound waves have no harmful biological side effect on the tissue [29]. In addition, ultrasound imaging can be performed at real-time rates. This enables observation of the fast moving structures such as the heart. Furthermore, because of the small-sized and flexible structures of the ultrasound imaging tools, they can be easily handled and used to image any part of the body. As a result of these, ultrasound have been widely used as a diagnostic tool for imaging of cardiac structures, vascular system, abdominal organs, eye, etc.

Tissue	Speed (m/sec)	Attenuation dB/cm/MHz	Impedance (Rayls)
Water	1480	0.0025	1.48
Air	330	12.0	0.0004
Fat	1410-1470	0.35-0.78	1.34-1.39
Soft Tissue	1540	0.81	1.62
Liver	1550	0.95	1.66
Kidney	1560	1.1	1.63
Muscle	1590	1.5-3.3	1.71
Spleen	1550	0.52	1.65
Bone	4080	12	7.8

Table 2.1: Sound parameters in different tissues.

In pulse-echo (reflection) mode ultrasound imaging, an ultrasound pulse composed of a few cycles is transmitted into the tissue, and the reflected waves are received. Reflection depends on the characteristic acoustic impedance of the tissue: impedance mismatch results in reflection. This allows to image the organ boundaries since generally different tissues have varying characteristic acoustic impedance [2] (Table 2.1).

In transmission and reception of the ultrasound pulses, piezoelectric transducers are used. Piezoelectric material is a polycrystalline ceramic that converts electrical signals to acoustic waves and vice versa. In ultrasound imaging, transducers are directly placed on the skin surface.

2.1 Phased Array Beamforming

A linear phased array consists of a number of transducer elements aligned side by side on a straight line [3, 30]. All array elements are active both in transmit and receive modes. Ultrasound signals transmitted or received from the array elements can be steered at a direction and focused at a point in that direction by adjusting element delay times to compensate the different round-trip times. In

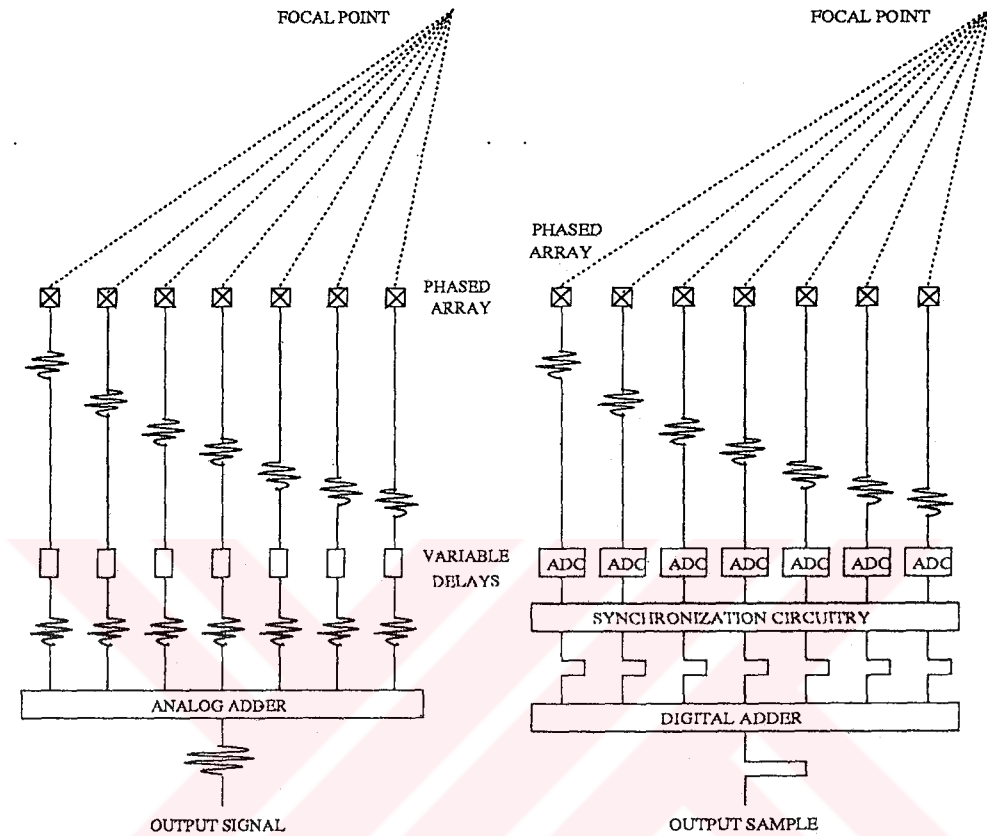


Figure 2.1: Symbolic representations of analog and digital receive beamforming schemes.

ultrasound imaging, beamforming is handled electronically using a phased array with variable delays (Fig. 2.1).

The scanning of the image plane is achieved by means of the transmit and receive beamforming operations. Transmit beamforming is achieved by sending appropriately delayed pulses while the receive beamforming is performed by properly delaying the received signals and summing them (Fig. 2.1). The transmit beamforming operation is carried out at each direction (i.e., per scan angle) while the receive beamforming is performed at each image sample point, which is called *dynamic focusing*.

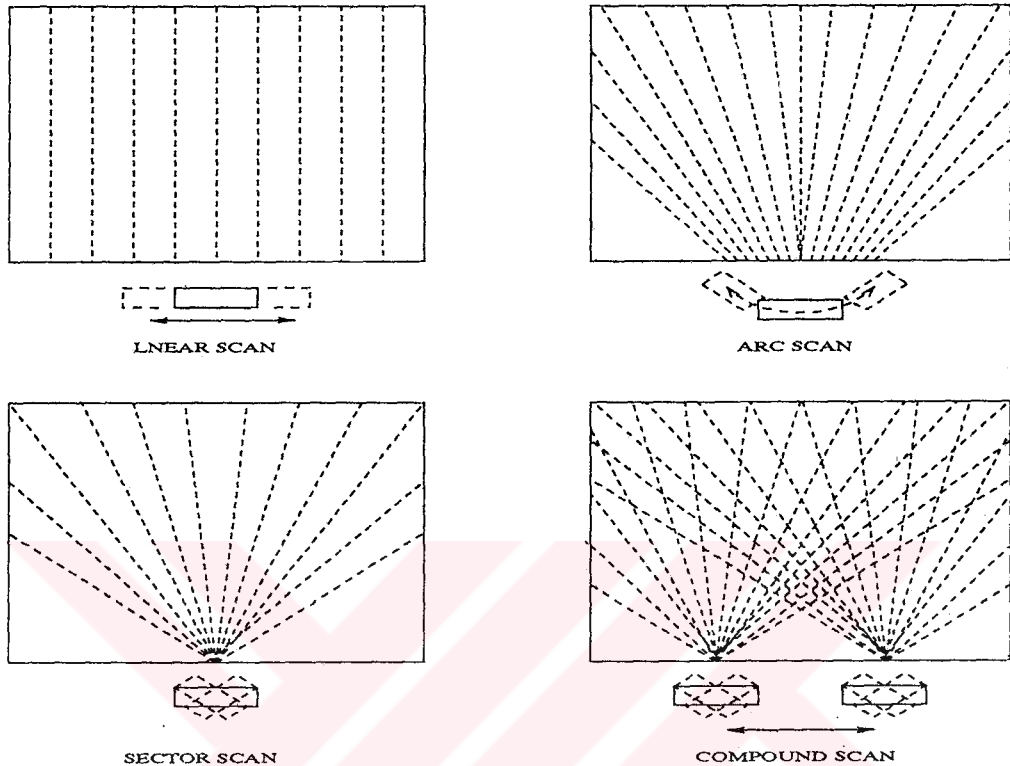


Figure 2.2: Scanning techniques in ultrasound imaging.

2.2 B-Mode Sector Imaging

The most common type of ultrasound imaging is the pulse-echo brightness mode scanning, called *B-mode* (also called *B-scan*) which provides a two dimensional cross sectional reflection image of the scanned tissue. A B-scan image is formed by sweeping a narrow pencil beam through a plane, and received signals from the sample points lying on the beam are mapped on an image corresponding to the place of beam on the plane. The next beam is sent to another portion of the plane after a time delay required for the previous beam round trip. This is repeated for all portions of the plane, and complete image of the region is obtained [4, 6].

The scanning of an imaging region is performed mainly in four ways (see Fig. 2.2). These are linear, sector, arc, and compound scanning [2]. Generally, the linear, sector, and compound scanning are performed by means of electronic

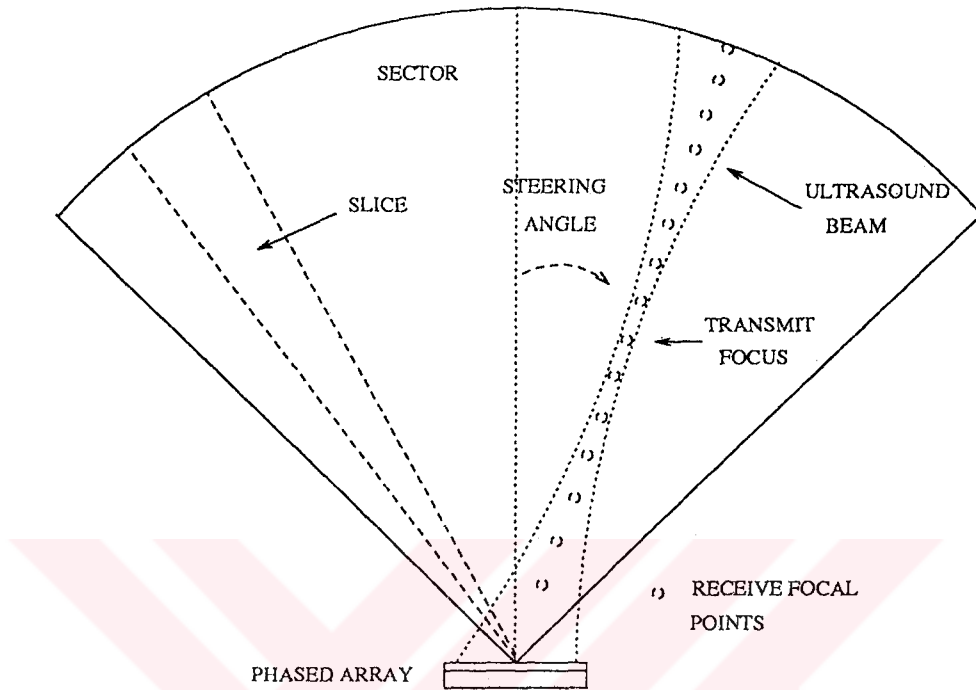


Figure 2.3: Phased array sector scanning.

scanning systems whereas the arc scanning is usually performed by mechanical scanning systems. In the sector scanning technique, the image plane is scanned in a sector format by steering the ultrasound beam in discrete angles within the sector (Fig. 2.3). Reconstruction of the sector image is achieved by performing receive focusing at each sample point lying on the axis of transmitted beam. Since the sector is scanned by means of the electronic beam steering, the physical aperture size of the transducer phased array is smaller compared to other scanner types, that allows observation of anatomic structures through restricted acoustic windows. As a result of this, sector scanners are widely used in medical imaging, especially in the cardiological diagnosis.

B-mode ultrasound sector imaging is based on the principle that only one sound pulse should be propagating in the field being scanned at any time. Hence, once a pulse is transmitted, the next pulse must be sent after the time required for round-trip of the previous pulse. This fact imposes a constraint for real-time systems such that $(Frame\ Rate) \times (Sector\ Radius) \times (No.\ of\ Scan\ Lines) =$

$c/2$. As a result of this, for a typical real-time imaging system with 30 frames/sec and 128 scan lines, the processing time per sample is about 250 nsec.

2.3 Ultrasound Image Resolution

Resolution of the ultrasound image is a measure of its ability to separate closely spaced individual structures. The resolution of an ultrasound imaging system depends on the shape of the ultrasound beam which is controlled by transducer array element spacing, number of elements, element weighting, pulse waveform, and the receiver response [31, 13, 21]. The axial resolution is mainly determined by the ultrasound pulse waveform (i.e., its frequency and pulse width) whereas the lateral resolution is closely related to the beamwidth (i.e., array size, element spacing, frequency and apodization). Most commonly used measures for ultrasound resolution are “full-width half-maximum” (FWHM), equivalently -6 dB, and -3 dB beamwidths [1].

Intensity of ultrasound pulse transmitted into the tissue is attenuated linearly proportional to the distance. While the attenuation increases with frequency thus limiting the penetration depth, the image resolution is directly proportional to the ultrasound frequency. Hence, the selection of depth and resolution of the image is a tradeoff in ultrasound imaging. In the applications, different frequencies are used for imaging of structures with various depth; 2.5-3.5 MHz for deep abdominal imaging, 5 MHz for imaging of organs near the surface and pediatric work, and 5-15 MHz for imaging of thyroid, testicles, peripheral vascular vessels, and eye.

Ultrasound image quality is critically affected by various factors such as quantization errors, scan-conversion process, phase aberration, inoperable array elements, and specular interference [18]. Enhancement of information content in ultrasonic images necessitates elimination or reduction of such quality limiting factors [32]. The first three problems are considered in detail throughout this study whereas the last two problems are briefly discussed and addressed as the further research issues.

Chapter 3

Digital Beamforming

3.1 Front-End Architecture

In phased array digital receive beamforming, RF echo signals received by the phased array elements are sampled using ADC's and then all signal processing operations are handled by digital electronics. An architecture showing the processing units for the digital front-end is depicted in Fig. 3.1. The timing accuracy in beamforming and in phase aberration correction is increased by upsampling. The phase aberration estimation is performed on the sampled data and then it is used to correct the beamforming timing computed for the receive focal points and transmit focus. The resampling process prior to beamforming is required to select the samples corresponding to the focal point. Finally, the samples corresponding to the focal point are synchronized and added to complete the beamforming. The signal value corresponding to the focal point is obtained at the output of the beamformer unit. The main difficulty in realization of this front-end is the requirement of relatively high sampling rate. In the following section, we discuss digital upsampling schemes to overcome this difficulty.

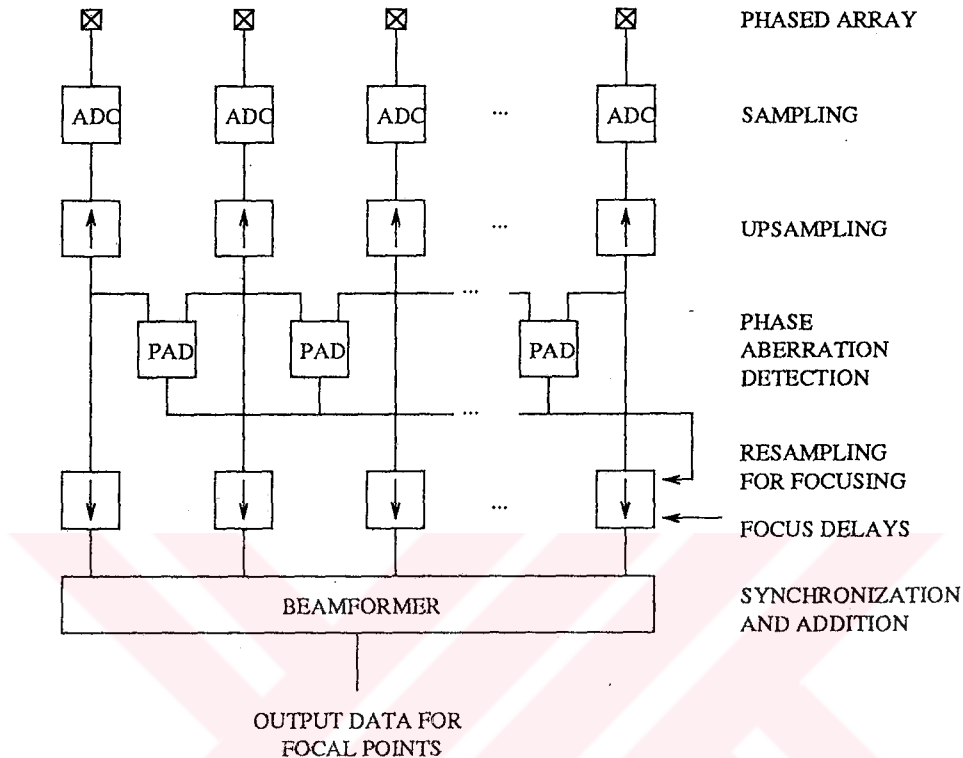


Figure 3.1: Digital receive front-end architecture.

3.2 Reduction of Delay Quantization Error

The amplitude quantization arising from the finite word length of analog to digital converters, reduces the dynamic range of the image signal [21, 33]. For pulse echo imaging, an 8-bit amplitude resolution is adequate whereas flow imaging applications require about 12-bit amplitude resolution [28]. These amplitude requirements are already met by the present ADC circuits. On the other hand, the delay quantization has a significant undesired effect on the transmit and receive responses of the system [20, 21, 22, 23]. The delay quantization results in an increase in the side lobe levels of the array response. Since the delay quantization is the most significant quantization error source, the major limitation in the digital front-end architectures is the timing accuracy, i.e., sampling rate of ADC's. As a general rule, a maximum phase error of $\pi/4$ is tolerable for phase array systems as long as the number of array elements is larger than 16 [30, 23].

In real-time imaging, accuracy of timing information used in beamforming based on the delay and sum, can be increased using fast ADC's with relatively high cost [34]. The sampling rate can be increased using baseband demodulation or bandpass interpolation techniques [35, 36, 37, 38, 14]. The realization of the former technique requires mixing and lowpass filtering, while the later requires only interpolation (zero padding and filtering). For the bandpass interpolation, to decrease the cost, one can employ zero padding on each channel signal before beamforming, and the interpolation filtering after beamforming [35, 36]. However, this scheme is not applicable for adaptive beamforming where the phase aberration correction is employed. Since the level of time quantization is much more critical than the level of the amplitude quantization [21, 23], a simple upsampling scheme such as a linear interpolation can be employed as a cost-effective solution to increase the timing accuracy.

3.2.1 Interpolation Scheme

In the linear interpolation, a new sample, point C , between two existing sample points, A and B , can be interpolated as

$$C = \frac{T_1 A + (T_2 - T_1) B}{T_2} \quad (3.1)$$

where T_1 and T_2 are the temporal distances between C and B , and A and B , respectively. For hardware realization, this expression can be further simplified by expressing the coefficients T_1 and T_2 in the sum of powers-of-two form [24]. To do that we need to quantize T_1 and T_2 . Eight equidistant interpolation points in each sampling interval, $T_2 = 8$, is tolerable for both the beamforming and phase aberration correction [30, 23]. Coefficients T_1 and T_2 can be expressed as

$$T_1 = 2^{p_1} + (-1)^{s_1} 2^{q_1} \quad T_2 = 2^{p_2} + (-1)^{s_2} 2^{q_2} \quad (3.2)$$

where p_1 , q_1 , s_1 , p_2 , q_2 , and s_2 are non-negative integer numbers depicted in Table 3.1. As a result, the realization of the interpolation is reduced to three shift and three addition operations.

T_1	p_1	q_1	s_1	p_2	q_2	s_2
0	0	0	1	2	2	0
1	1	0	1	3	0	1
2	0	0	0	2	1	0
3	1	0	0	2	0	0
4	1	1	0	1	1	0
5	2	0	0	1	0	0
6	2	1	0	0	0	0
7	3	0	1	1	0	1

Table 3.1: Powers of 2 for T_1 and $8 - T_1$.

3.2.2 Hardware Structure for Interpolator

The hardware structure shown in Fig. 3.2 is developed for the linear interpolation scheme. It takes two input samples, A , and B , and the value of time distance to the point at which the interpolation will be performed. It generates the interpolated sample, C , as its output. The power coefficients for representation of T_1 and $T_2 - T_1$, are generated by decoding T_1 . The resultant signals, p_1 , q_1 , s_1 , p_2 , q_2 , and s_2 , are used as the control signals for “shift left” operations on the input samples. Then, the appropriately shifted versions of each sample are added to realize the multiplications,

$$T_1 A = (2^{p_1} + (-1)^{s_1} 2^{q_1}) A \quad (T_2 - T_1) B = (2^{p_2} + (-1)^{s_2} 2^{q_2}) B \quad (3.3)$$

Then, the interpolated sample is obtained by adding these two results and performing a shift right operation on the output. The interpolator scheme is designed in five pipelined levels to achieve a high throughput.

3.3 Beamforming at Raster Focal Points

In conventional phased array ultrasound imaging, the radial data are converted to the raster format using digital scan-conversion techniques [25]. A typical digital scan converter maps the radial data to the nearest display pixel.

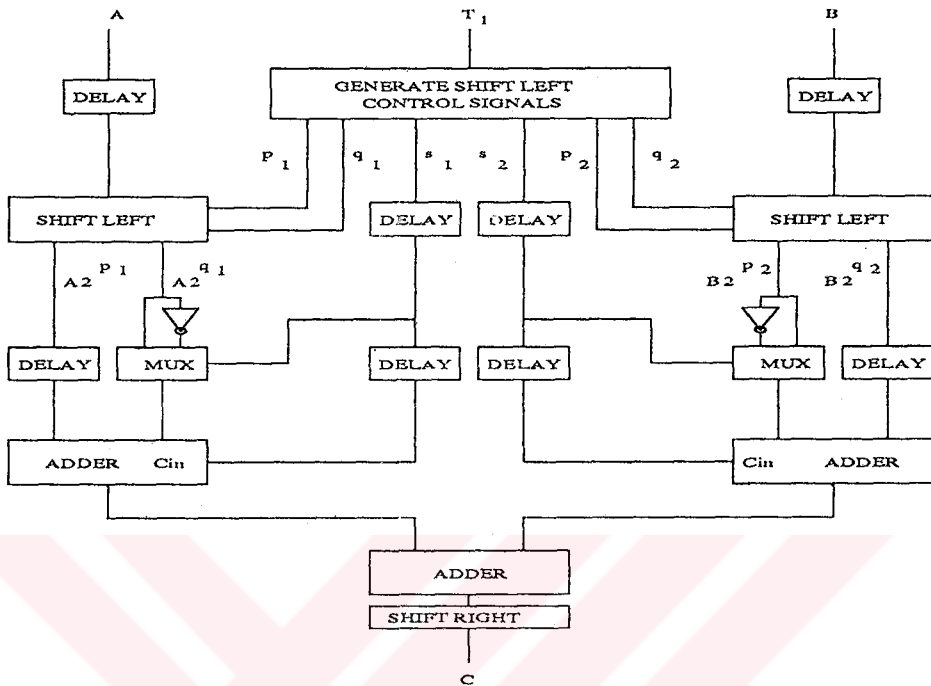


Figure 3.2: Hardware structure of the linear interpolator.

This corresponds to the quantization of the radial coordinates to the nearest rectangular coordinates (see Fig. 3.3), where the data is forced into alignment with the display grid. Thus, it results in an annoying artifact called Moire pattern which is a well-defined pattern of holes in the image corresponding to the unaddressed pixels. Artifacts can be decreased by using two dimensional interpolation techniques [39, 34]. However, this significantly increases the computational cost of the scan conversion process.

The conversion process can be completely eliminated by performing the receive beamforming operations directly at the raster focal points of the imaging plane instead of the radial focal points [40, 41]. Image reconstruction at the raster sample points can be accomplished by forming transmit beams at unequal angles so that raster points lie on the beam axis, and sample unequally in time along the beam that correspond to raster lines. However, amount of time to form all these transmit beams is too long for real-time imaging.

As an alternative approach, we form transmit beams at equal angles and

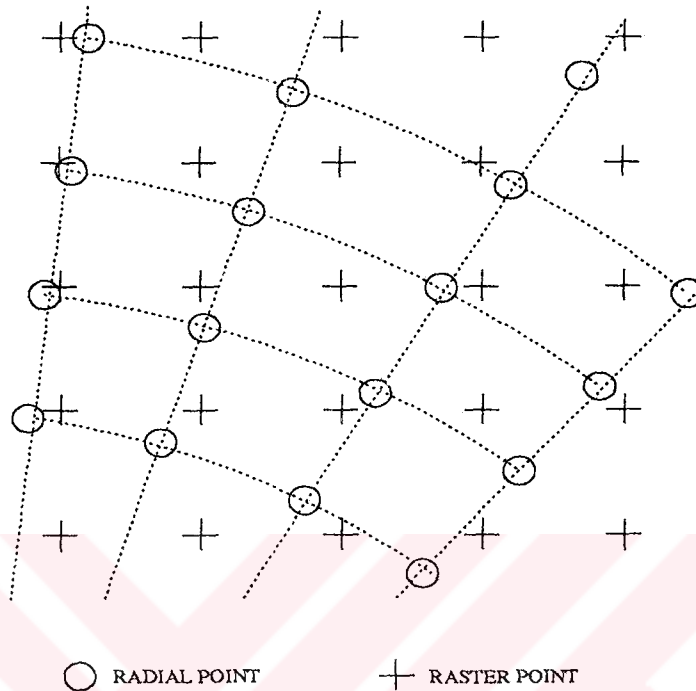


Figure 3.3: Radial and raster focal points.

sample the beam at the times corresponding to the raster focal points within the scan angle. To do this, the timing data required for the receive beamforming must be computed for every raster focal point at every scan angle within the sector. Since the number of raster points in the sector is about 2.5 times the number of radial points, the number of receive beamforming operations increases by the same amount. This is a major reason why the many phased array systems have employed beamforming at the radial focal points. It is not a limitation for synthetic aperture imaging schemes [38], but the synthetic aperture imaging technique is not preferred in medical imaging because of the SNR and real-time operation requirements. In phased array imaging at the raster points, the computational overhead due to the increased beamforming operations can be effectively handled by employing digital beamforming schemes.

3.3.1 Performance Analysis

For the analysis of the beamforming at radial and raster focal points, the point spread functions (PSF) and sector images of an ultrasound resolution phantom are obtained and compared. The PSF's are formed by means of computer simulation whereas the phantom images are reconstructed by digital processing of an experimental RF data set acquired from a tissue-mimicking resolution phantom.

PSF SIMULATIONS

Various computer simulation models for ultrasound imaging, that involve involve complex computations for simulation of system and tissue parameters, have been investigated [42, 43]. For the PSF simulations, because of the computer run time requirements, we use a simple simulation model in which the attenuation and cylindrical spreading effect are not included. In the simulations, overall sample value of the signal corresponding to the receive focal point (p, q) , $s(p, q)$, is obtained as

$$s(p, q) = \sum_{n=1}^N w_n \sum_{k=1}^N w_k \sum_{i,j} G(n, i, j) G(k, i, j) R(n, k, i, j) P(t_s(n, p, q) - t_r(n, k, i, j)) \quad (3.4)$$

where, N is the number of array elements, w_i is the apodization coefficient, $G(\cdot)$ is the element factor, $R(\cdot)$ is the reflectivity coefficient, $P(\cdot)$ is the transmitted ultrasound pulse, $t_s(\cdot)$ is the sampling time, and $t_r(\cdot)$ is the round-trip time including the transmit delay. In the above expression, the summation over i and j represents the specular contributions of whole field, whereas the summations with index k and n correspond to the transmit and receive processes.

The ultrasound pulse, $p(\cdot)$, for each element is assumed to be identical and in the form of a Gaussian pulse expressed as

$$P(t) = e^{-(t/2T_0)^2} e^{j2\pi f_0 t} \quad (3.5)$$

where f_0 and T_0 are the ultrasound frequency and period, respectively.

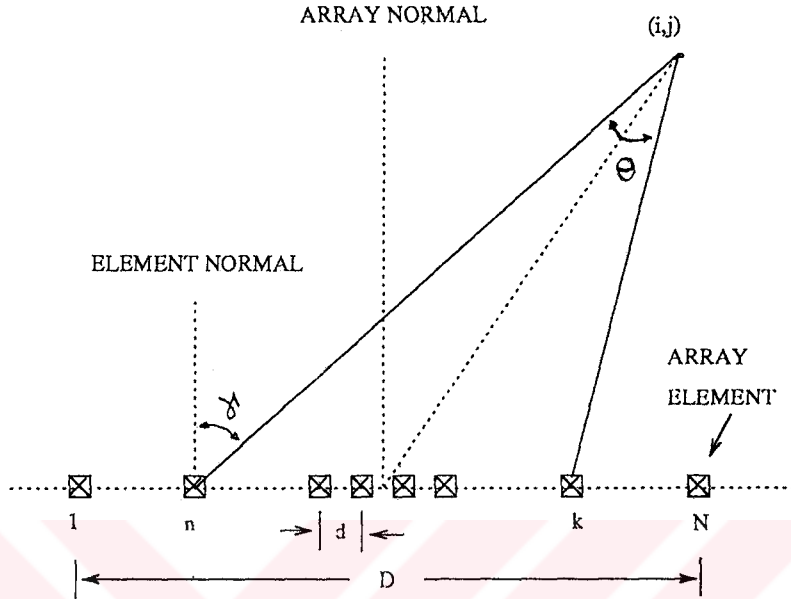


Figure 3.4: Geometrical configuration for the simulation parameters.

Since the array element is not a point source, and has a finite size, the element transmit/receive response is directional. This is represented as [44]

$$g(n, i, j) = \frac{\sin(\pi \sin(\gamma(n, i, j)))}{\pi \sin(\gamma(n, i, j))} \quad (3.6)$$

where $\gamma(n, i, j)$ is the angle between element normal and the line joining the center of element and the scattering point (i, j) (see Fig. 3.4). Here, the element size is assumed to be half of a wavelength.

To obtain the PSF for the point reflector located at (i_0, j_0) , the reflectivity function can be expressed as:

$$R(n, k, i, j) = \delta(i - i_0, j - j_0) \cos(\theta(n, k, i_0, j_0)) \quad (3.7)$$

where the $\delta(\cdot)$ is the Kronecker delta function and the $\theta(\cdot)$ is the scattering angle used to represent the specular reflectivity (see Fig. 3.4). The other simulation parameters are as follows: $N = 128$, the number of scan-slices/ 90° -sector is 128, and the time is quantized by $T_0/8$.

The PSF's obtained by beamforming at the radial and raster points are shown in Fig. 3.5 where each figure depicts two dimensional distribution of the

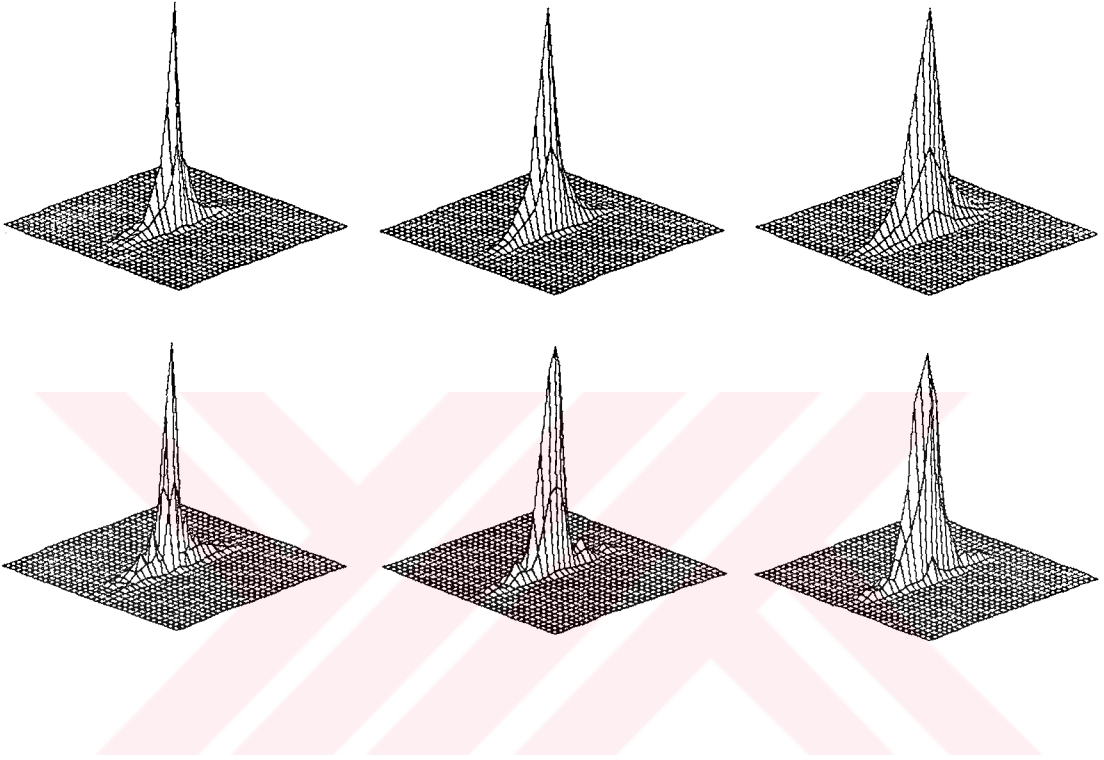


Figure 3.5: Normalized PSF magnitude. The PSF’s in the first and second rows are obtained by beamforming at radial and raster focal points, respectively. The PSF at the first, second and third columns correspond to the point reflectors located at $2D$, $4D$, and $6D$ away from the array, respectively.

Distance	(2D)			(4D)			(6D)		
- dB	6	10	40	6	20	40	6	20	40
Radial	4	10	20	4	12	20	12	22	30
Raster	4	8	18	4	8	16	8	12	26

Table 3.2: PSF beamwidths normalized by the ultrasound wavelength. FWHM beamwidth corresponds to -6 dB beamwidth.

normalized PSF magnitude on a $32\lambda_0 \times 32\lambda_0$ window where λ_0 is the ultrasound

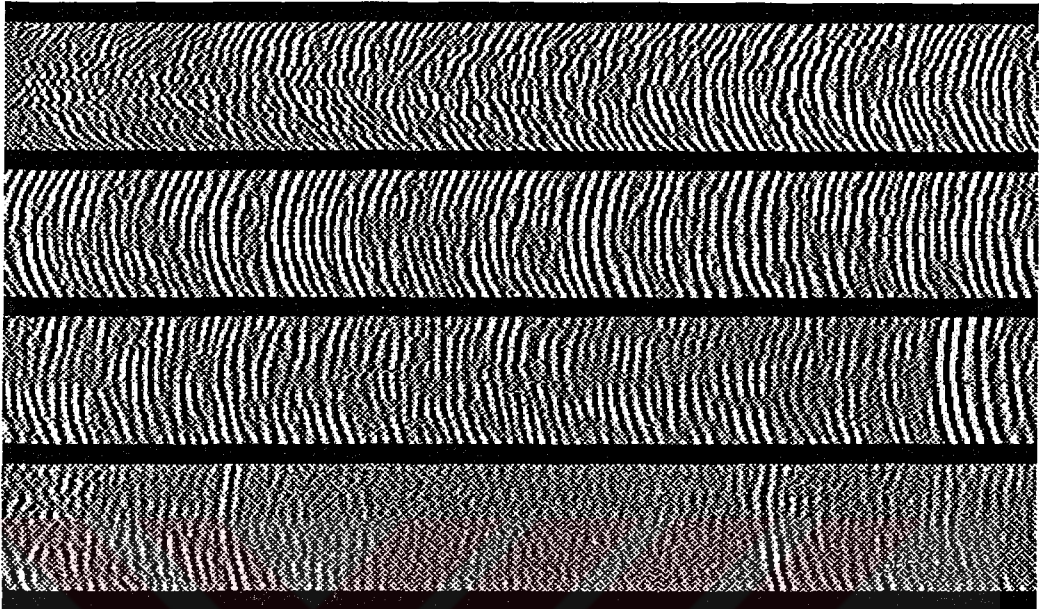


Figure 3.6: Received experimental RF wavefronts across the array. The vertical and horizontal widths of each row correspond to the aperture size and time interval of 512 samples, respectively. The first, second, third and fourth rows show the samples between 1-512, 513-1024, 1025-1536, 1537-2048, respectively.

wavelength. The beam-widths comparisons of PSF's are given in the Table 3.2. In the PSF simulations, transmit focal length is fixed to $6D$, where D is the aperture size of the array, and the point reflector is located at $2D$, $4D$, and $6D$ away from the array, placed on the axis normal to the array. For the apodization of array, Blackman and rectangular windows are used at transmit and receive modes, respectively.

The PSF's shown in Fig. 3.5 and the Table 3.2 indicate that the resolution obtained by beamforming at the raster sample points is better than that beamforming at the radial sample points.

RECONSTRUCTION OF THE PHANTOM IMAGES

To compare the image qualities of receive beamforming at the radial and raster focal points, the sector images of the standard graphite-gel AIUM image resolution phantom are reconstructed using the two beamforming techniques.

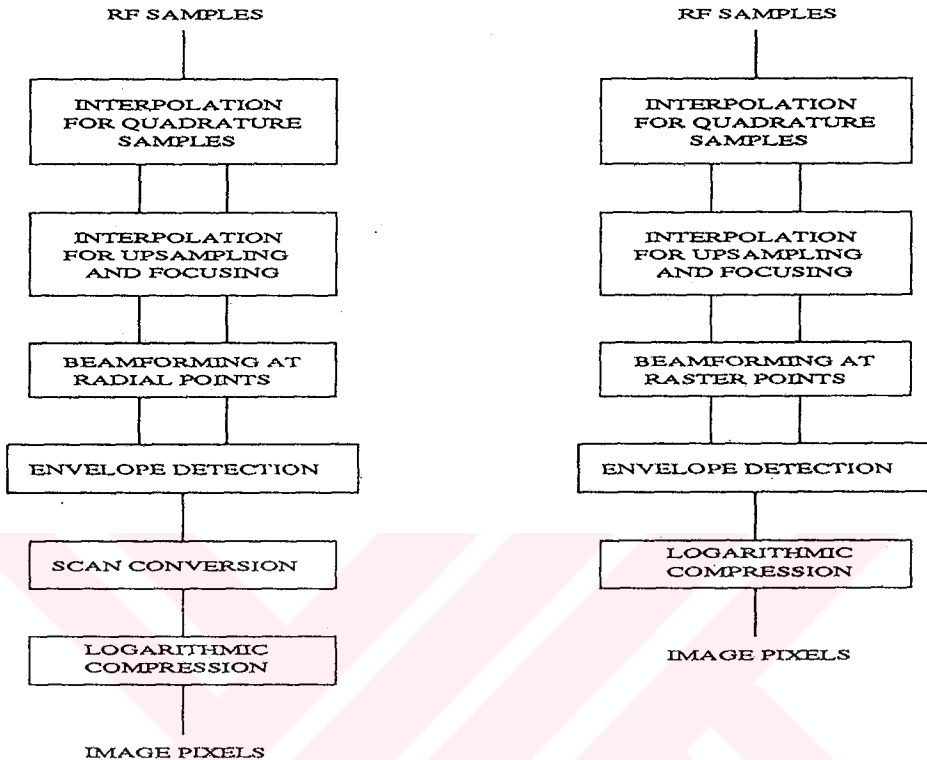


Figure 3.7: Digital processing steps for beamforming at radial and raster points.

The actual RF data set[†] was acquired from the phantom with a conventional 64-element phased array transducer operating at 3.3 MHz [45, 46]. The data acquisition was carried out through the synthetic aperture scheme such that all of the RF A-scans were recorded for every possible combinations of transmitter and receiver elements. Each A-scan was digitized after appropriate time gain compensation at a sampling rate of 17.76 MHz with 10-bit analog to digital conversion. The data file occupies about a 34 Mega bytes of storage in the computer memory. Fig. 3.6 depicts the received wavefronts across the array where a portion of the RF data set is shown for a particular transmit beamforming at a scan angle normal to the array aperture.

Image reconstruction is carried out by digitally processing the recorded synthetic aperture data to emulate the operation of a real-time digital imaging

[†]Provided by Prof. Matthew O'Donnell of Michigan University.

system. The sampling rate of RF data is increased further by 8 times using the linear interpolation scheme discussed previously, and the quadrature signal components are generated. The digital processing schemes for beamforming at radial and raster points are outlined in Fig. 3.7. The beamforming is performed using timing data computed for radial and raster receive focal points. The envelope detection is realized by taking the square root of the sum of the squares of in-phase and quadrature samples. The scan conversion which is employed in beamforming at the radial points, is realized using a first order two dimensional interpolation technique presented in [39]. This interpolation scheme is also depicted in Fig. 3.8. Finally, a purely logarithmic compression is applied on the images to obtain a 60 dB dynamic range.

In the image reconstruction, the separation of the raster and radial focal points are chosen to be $\lambda_0/2 = 0.23$ mm. The number of scan-slices/90°-sector is 128. The images consist of 512×512 pixels (Fig. 3.9). The transmit focal length is fixed at 80 mm away from the array, which corresponds to the position of the point reflector at center of the sector. It is observed from these images that the image obtained by beamforming at radial points is blurred due to the scan conversion. A detectable resolution improvement is achieved by employing the receive beamforming at the raster focal points.

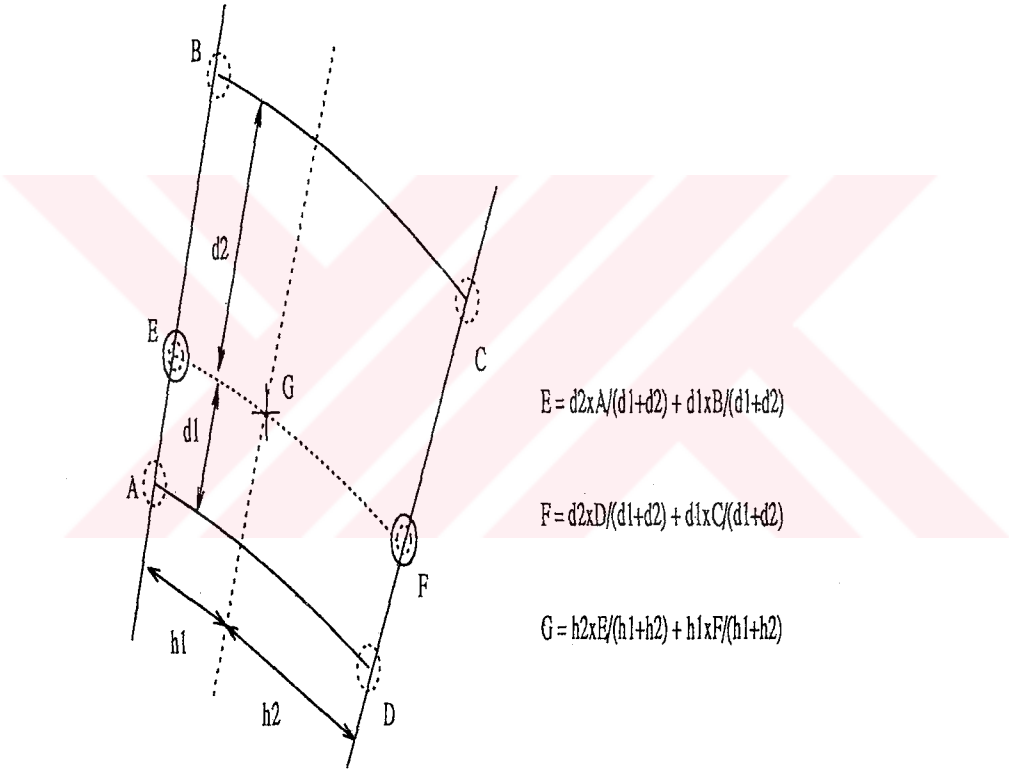


Figure 3.8: Interpolation scheme used in the scan-conversion.

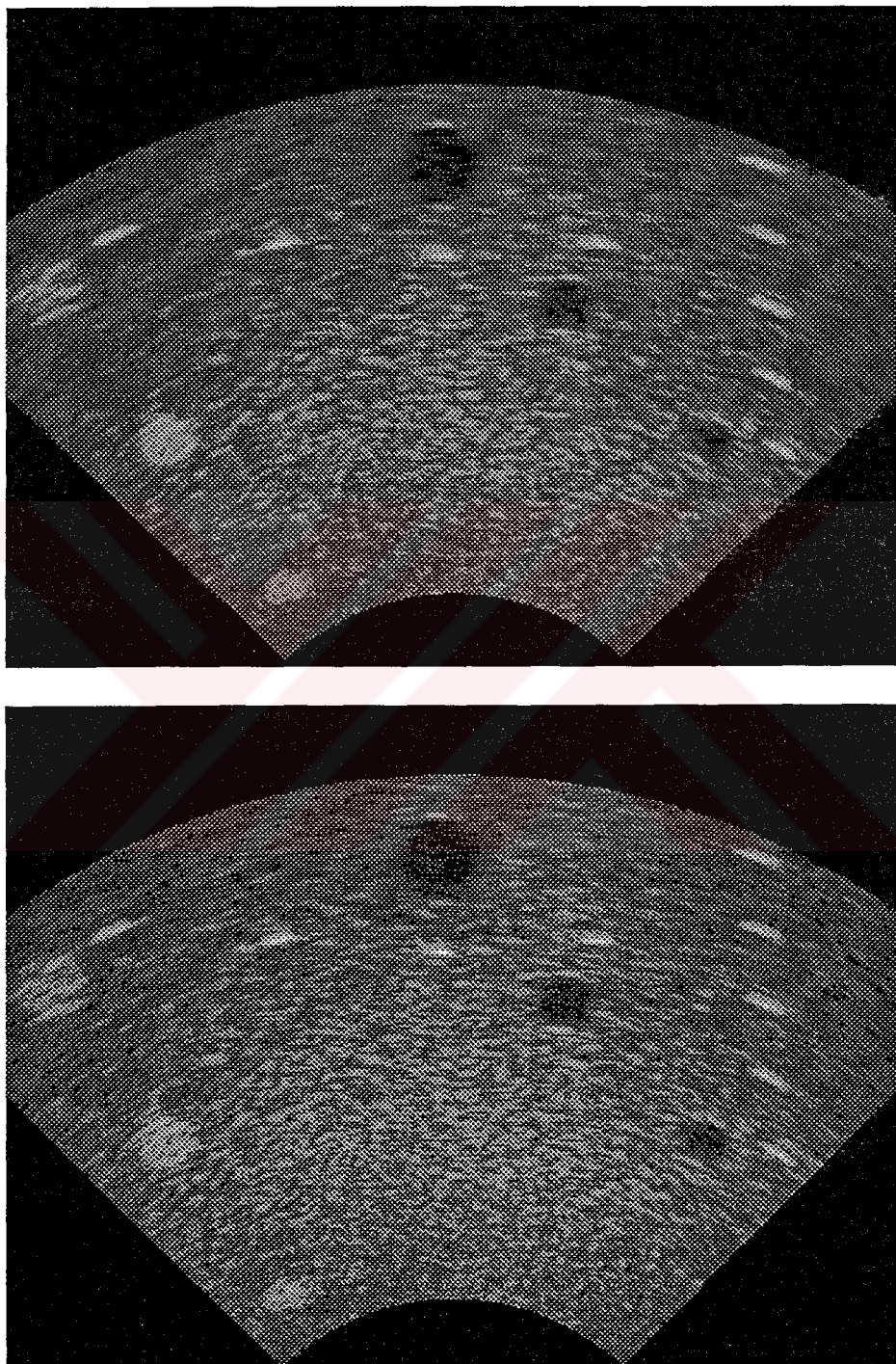


Figure 3.9: Ultrasound sector images of the standard graphite-gel AIUM resolution phantom. The top and bottom images are reconstructed by receive beamforming at radial and raster points, respectively, through the digital processing steps depicted in Fig. 3.7.

3.3.2 Hardware Structure for Digital Beamformer

In digital receive beamforming, the samples corresponding to a focal point are not synchronous. In order to find the signal value of a focal point, the samples must be suitably delayed and then added. This requires coherent addition of signals received by the array elements. However, a simple synchronization scheme designed for a regular data flow structure can not solve the synchronization problem in receive beamforming for sector imaging. This is due to the fact that the arrival time pattern of samples varies depending on the location of focal point within the sector.

In a straightforward approach, a “global” coherent summation scheme can be employed by using FIFO type registers at the adder front-end [47, 14, 48, 23]: the samples from all channels are stacked in FIFO registers at each channel for synchronization, and then the synchronized data corresponding to a focal point are added to obtain the beamformer output. However, since the FIFO and adder sizes increase dramatically with the number array of elements, the scheme is not very feasible for implementation at the board level or in VLSI. Alternatively, the samples can be added recursively using partial sum registers [34]. But this technique is not particularly practical, because of the adder speed requirement.

An efficient receive beamforming hardware structure can be obtained by employing a “local” coherent addition technique where the total coherent summation of all samples corresponding to a focal point is obtained by a sequence of pairwise partial coherent summations [49, 50, 51]. For an N channel system, at first, $N/2$ partial coherent summations are obtained. Then, adjacent pairs of these partial sums are coherently added resulting in $N/4$ new partial coherent sums. This procedure is repeated until the number of new partial coherent sums becomes unity, which is the total coherent summations of all samples. This approach results in an inverse binary tree like architecture for receive beamformer. For an N element array, the network consists of $\log_2(N)$ stages, and k 'th stage has $N/2^k$ ($k = 1, 2, \dots, \log_2(N)$) processing units (see Fig. 3.10).

Each unit consists of FIFO registers and a full adder for coherent summation of its two input data. FIFO length for each stage is different; since there is

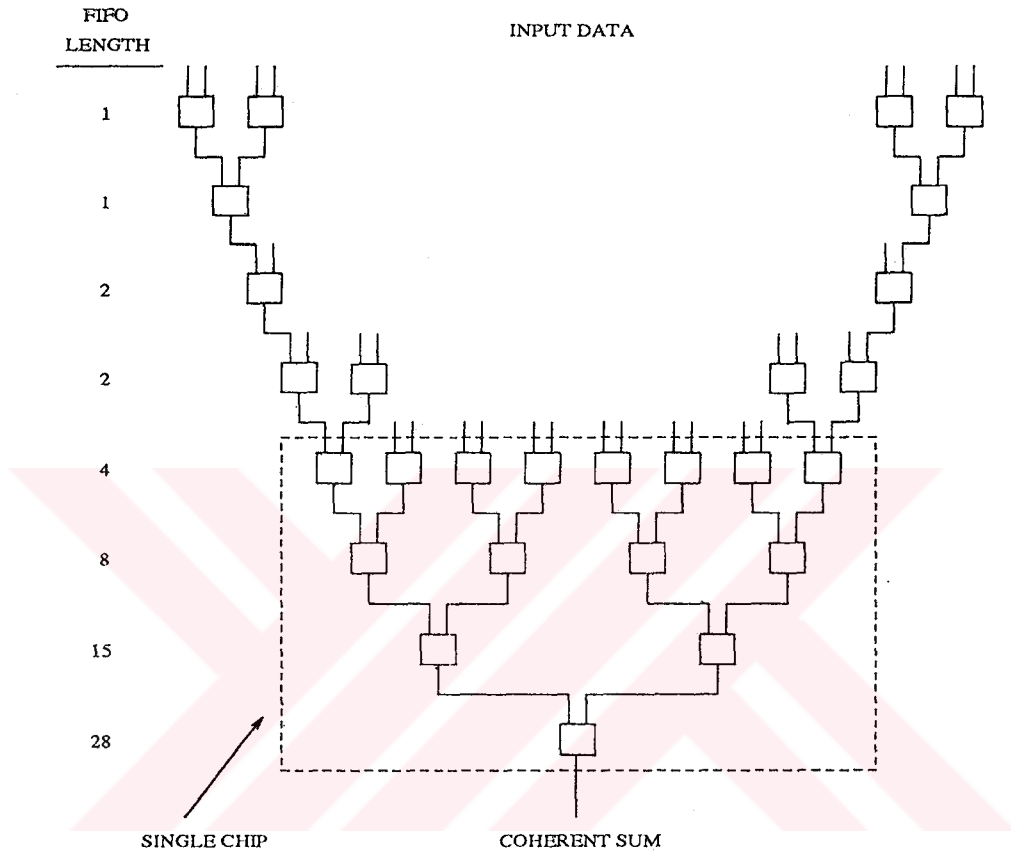


Figure 3.10: Architecture of the beamformer.

no regularity in the arrival times of the signals corresponding to different focal points, the worst case FIFO lengths for the stages are determined by means of the computer simulation of the phased array imaging system with a 90° sector scanning.

The processing unit takes two input data, A and B , along with two status bits, SA and SB , and generates the coherent summation of the inputs, DO , with a corresponding output status bit, SO (Fig. 3.11). Each status bit indicates that the data is valid. For a reliable real-time operation, the unit is designed in three pipelined stages : cross switch, FIFO, and adder stages. The cross switch is a finite state machine which feeds the earlier of the inputs, A or B , to the

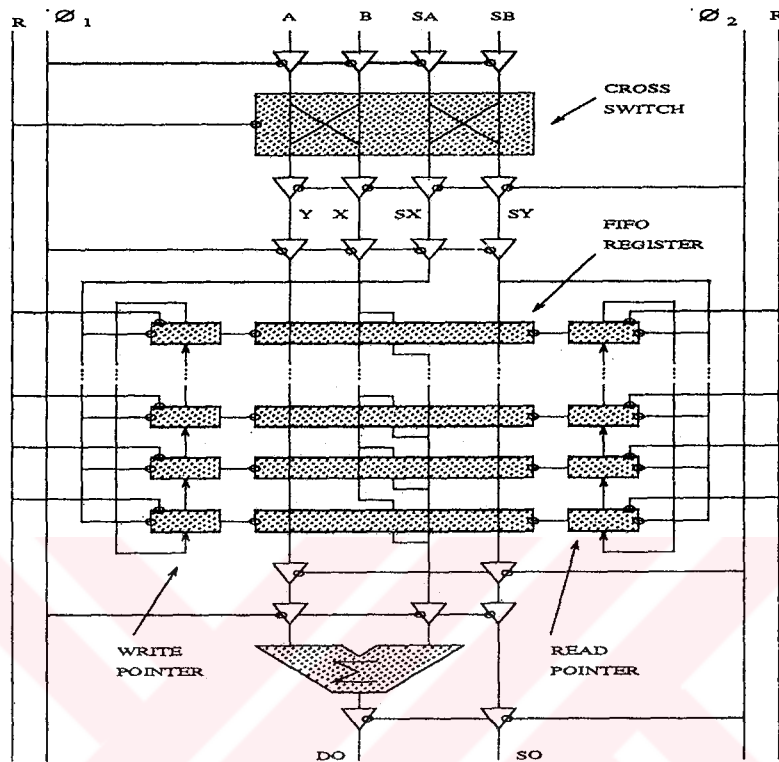


Figure 3.11: Functional structure of the processing unit.

subsequent FIFO. After synchronization by FIFO, the data are fed to the full adder. The unit is reset by an external reset signal (R) at the beginning of operation so that cross switch and FIFO pointers are set appropriately. Two non-overlapping clocks (ϕ_1 and ϕ_2) are used to control the pipelined operations and data flow.

3.4 Concluding Remarks

To reduce the delay quantization errors in beamforming by delay and sum operations, a cost effective upsampling scheme based on bandpass linear interpolation is presented together with its hardware structure.

By means of the simulated PSF's and the sector images of the phantom reconstructed from the experimental data, it is found that image reconstruction

by employing receive beamforming at the raster sample points results in a higher resolution compared to that for the radial sample points.

Beamforming directly at the raster points is not easy to realize in hardware due to increased focusing operations. Dynamic focusing to the raster points employing the digital beamforming schemes can be best implemented using special-purpose hardware structures [49, 52].

VLSI implementation of the proposed beamformer structure for large N is not very feasible because of the large chip area and large number of I/O's. The modularity of the structure can be employed effectively, however, by proper choice of FIFO sizes, and by using the beamformer chips with a reasonably small N [50].



Chapter 4

Phase Aberration Correction

4.1 Introduction

Phased array ultrasound sector images are reconstructed by employing beamforming operations both in transmit and receive modes. Timing considerations for beamforming are usually based on the assumption of constant sound velocity throughout the body. However, this assumption is not valid in general since the sound velocity varies in different tissues. For example, the velocity of sound is about 1440 m/s and 1560 m/s in fat and kidney, respectively, while it is 1540 m/s in soft tissue (Table 2.1). Changes in sound velocity, especially in the near field, cause significant phase errors in beamforming (Fig. 4.1). Measurement of the phase aberration and its effects on the image quality have been investigated experimentally [26, 27]. The image quality is critically affected by these phase errors which result in increased side lobes, degradation in resolution, and geometrical distortion (Fig. 4.2).

In medical ultrasound imaging, the relative phase errors in adjacent elements are in the form of perturbation and generally less than $\pi/4$. The phase aberration becomes a significant problem in imaging with relatively high frequency ultrasound, since the phase errors due to the aberration increases as the carrier frequency increases. For example, a phase aberrator causing a relative flight time difference of 40 nsec in adjacent elements results in a $0.1 \lambda_0$, $0.2 \lambda_0$,

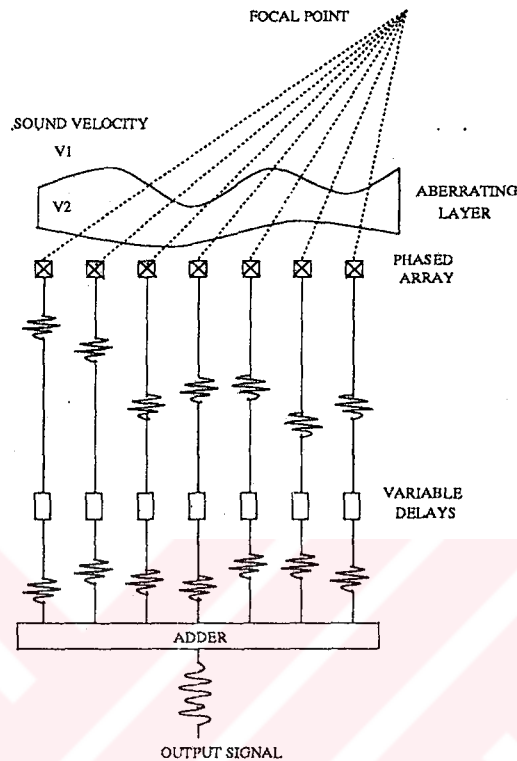


Figure 4.1: Symbolic representation of the phase aberration in receive beamforming.

and $0.4 \lambda_0$ phase shifts in 2.5 MHz, 5 MHz and in 10 MHz, respectively.

To insure optimal imaging, phase errors must be estimated and corrected adaptively in real-time. Use of a beacon signal for phase estimation, a conventional method in many coherent imaging systems [53], may not be possible in noninvasive medical imaging applications. This is because a point like target may not exist at every imaging plane of the body. Hence, a practical method must generate accurate estimates of phase errors using the signals from line targets and/or diffuse scatterers.

Phase aberration correction methods have been reported for a nonuniform aberrating layer with a deterministic target [54, 55], and for a uniform aberrating layer with a priori information about the layer thickness [56]. For nonuniform aberrating structures with random reflector distributions, various phase correction techniques have been reported which are based on the cross

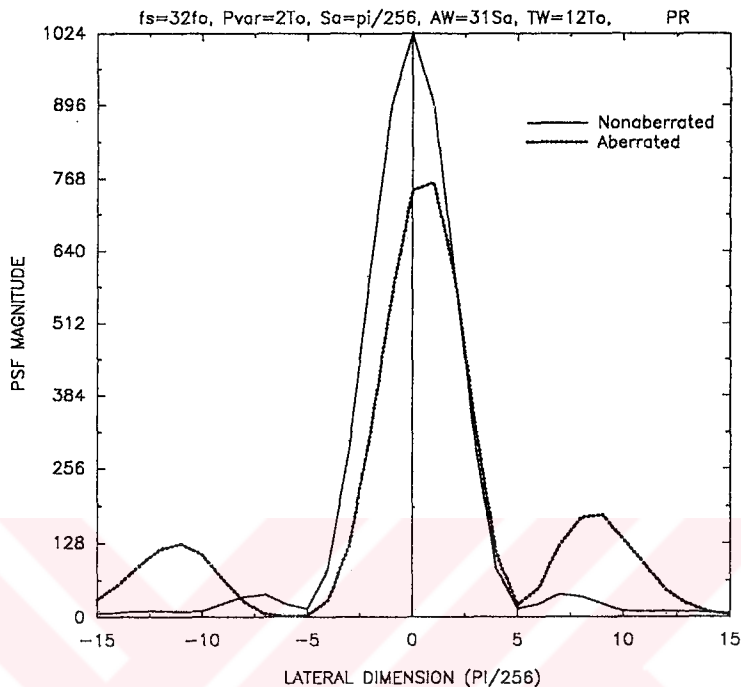


Figure 4.2: Effect of the phase aberration on PSF.

correlation between the sampled RF signals of adjacent elements [45, 46, 57, 58], on the maximization of the speckle brightness [59, 60, 61], and on the time reversal mirror [62, 63, 64]. Computational complexity of each of these schemes is relatively high for real-time imaging. Recently, two-dimensional phase aberration correction studies have been reported [65, 66, 67] which were extended versions of the one-dimensional correction schemes. Also, there exist time delay estimation techniques [68, 69, 70, 71] which involve extensive computations, and hence are more suitable for off-line phase correction. For real-time ultrasound imaging, however, the computational efficiency of the correction algorithm is crucial.

In this study, we present an alternative phase aberration correction technique with low computational complexity. The relative phase errors of adjacent array channels are estimated effectively through minimization of the sum of absolute differences (SAD) between two RF samples. In order to increase the accuracy and

convergence performance of the SAD technique, we employ weighted averaging of estimated patterns over a number of scan angles. The weighting coefficient for each angle is chosen as the average magnitude of the echo signal received at this angle. To increase the computational efficiency of the technique further, the word length is truncated to one bit.

4.2 Technique

4.2.1 Approach

SAD is used as a cost function in minimization problems because of its low computational complexity. It has been used as the alternative to the correlation and successfully applied for the image registration [72], pitch detection [73], flow and motion imaging [74], and for the non-linear filtering [75, 76].

We employ SAD for estimation of the relative phase difference between two sampled RF signals [51, 77]. SAD of RF echo samples received from adjacent array channels, over a time window of length M , is expressed as a function of shift index, r_n^i , as

$$\epsilon(r_n^i) = \sum_{k=1}^M |s_n^i(k) - s_{n-1}^i(k + r_n^i)| \quad (4.1)$$

where $s_n^i(k)$ is the k 'th sample of the n 'th element's signal at the i 'th scan angle. Typically, $s_n^i(\cdot)$ and $s_{n-1}^i(\cdot)$ are approximately shifted versions of each other. The value of r_n^i which minimizes this expression corresponds to the relative phase shift, and is found for every n and i (see Fig. 4.3). The relative aberration delay for the n 'th element at the i 'th scan angle, α_n^i , is given by

$$\alpha_n^i = T_s r_n^i - \gamma_n^i \quad (4.2)$$

where T_s is the sampling period, and γ_n^i is the relative focusing delay. The aberration delay time, τ_n^i for the n 'th element at the i 'th scan angle is the cumulative summation of the relative aberration delays:

$$\tau_n^i = \sum_{j=1}^n \alpha_j^i \quad (4.3)$$

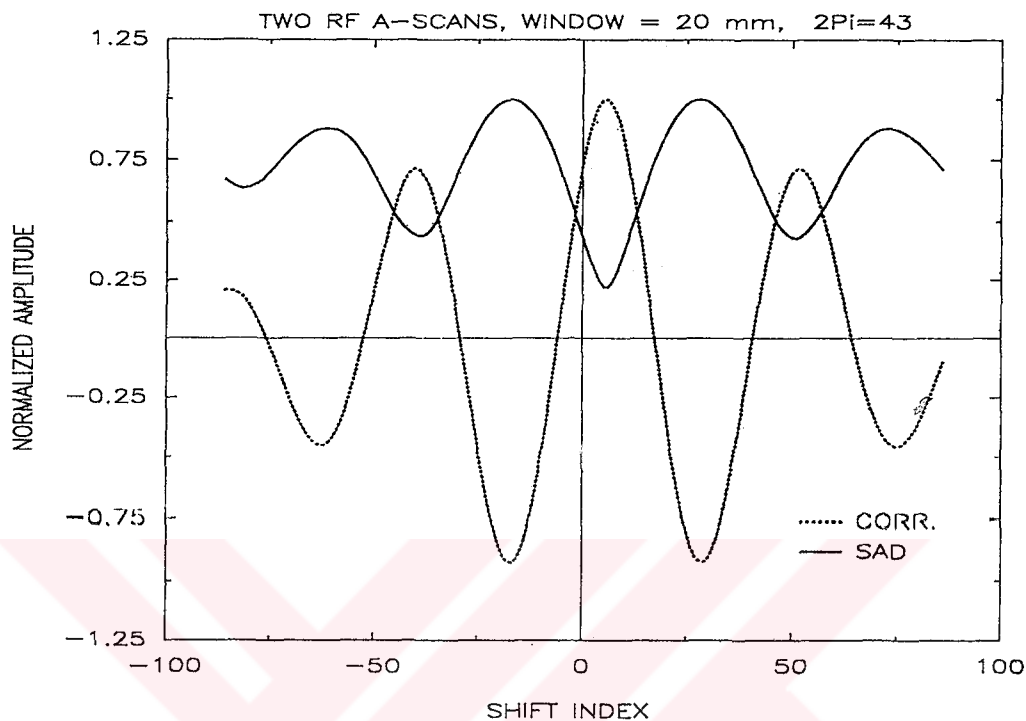


Figure 4.3: SAD and cross correlation of two sampled RF signals.

Analysis of the sensitivity of SAD to the relative phase, the accuracy of time delay estimation using SAD and correlation, and the spatial covariance of RF signals across the array measured with SAD and correlation are presented in the Appendices A, B, and C, respectively.

4.2.2 Averaging of Phase Estimates

Time delay estimation using simple SAD minimization can be used to measure phase distortions due to nonuniform aberrating layers. However, scatterers in the direction of sidelobes may also contribute to phase errors, which are referred to as phase aberration due to the “multipath and scattering” [78]. Depending on the scatterer distribution over the isoplanatic patch where the phase estimation is carried out, the effect of multipath and scattering may not cancel out, resulting in focusing errors. Such phase errors may affect the accuracy and convergence

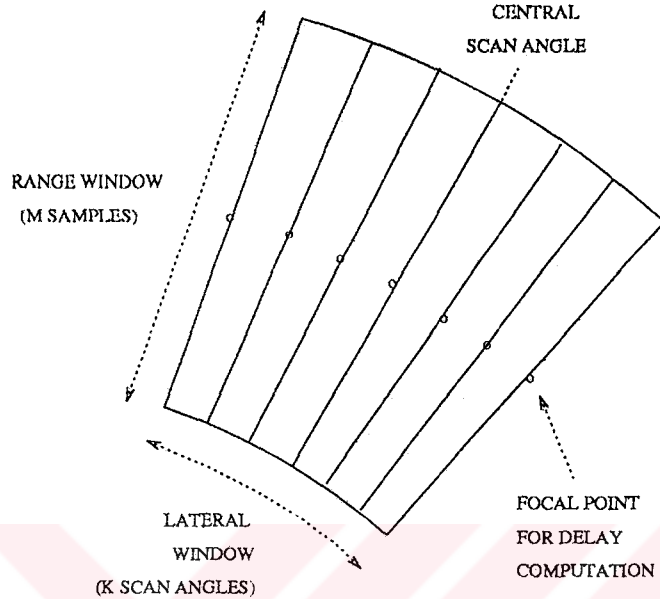


Figure 4.4: Window configuration used for two dimensional SAD minimization.

performance of the aberration estimation. In order to reduce these errors, the estimation can be performed over a lateral window as well as over a time (axial) window (see Fig. 4.4). This can be achieved by minimization of SAD over a two-dimensional window (referred as 2-D SAD estimator) [77]. Another possibility is to minimize SAD and average the weighted estimates over a number of scan angles (referred as averaged SAD estimator) [77].

Because the echo signal is not uniform over angles, averaging of the estimated aberration delays over a two-dimensional window needs proper weighting. The weight coefficient of the n 'th array element, w_n^i , for the i 'th scan angle is defined as the average magnitude of the echo signal received from this element, i.e.,

$$w_n^i = \frac{1}{M} \sum_{k=1}^M |s_n^i(k)| \quad (4.4)$$

Either a unique weighting for each element or a single weighting bound on the average magnitude over all elements can be used. This weighting scheme biases the estimation to scan angles where relatively strong reflections are detected. It requires a simple operation. The weighted average of estimated aberration delays

	2-D SAD	Averaged SAD
Point reflector	0.20	0.05
Uniformly distributed random scatterers	0.38	0.11
Point reflector with -10 dB random scatterers	0.27	0.09

Table 4.1: RMS error between the estimated and actual aberration patterns (unit: fraction of a wavelength).

is expressed as

$$\bar{\tau}_n = \frac{\sum_{i=1}^K w_n^i \tau_n^i}{\sum_{i=1}^K w_n^i} \quad (4.5)$$

where K is the number of scan angles used for averaging, and $\bar{\tau}_n$ is the averaged aberration delay for n 'th element.

COMPARISON OF 2-D SAD AND AVERAGED SAD ESTIMATORS

To compare the performance of phase estimation with 2-D SAD minimization and SAD with averaging of weighted estimates, computer simulations for point and randomly distributed reflectors are performed [77, 51]. In the simulations, the simulation model previously described in Chapter 3 is employed. For the aberration, a random aberration delay pattern varying between $-\pi/4$ and $\pi/4$ is used. The simulations are performed at a region $3D$ away from the array, where D is the array aperture. The region where the error minimization is carried out consists of 31 scan angles, each of about 0.7° . The length of time window is $8T_o$, and the phase is quantized by $2\pi/32$.

RMS error between the estimated and actual aberration patterns for 2-D SAD and averaged SAD estimators for different reflector distributions are obtained

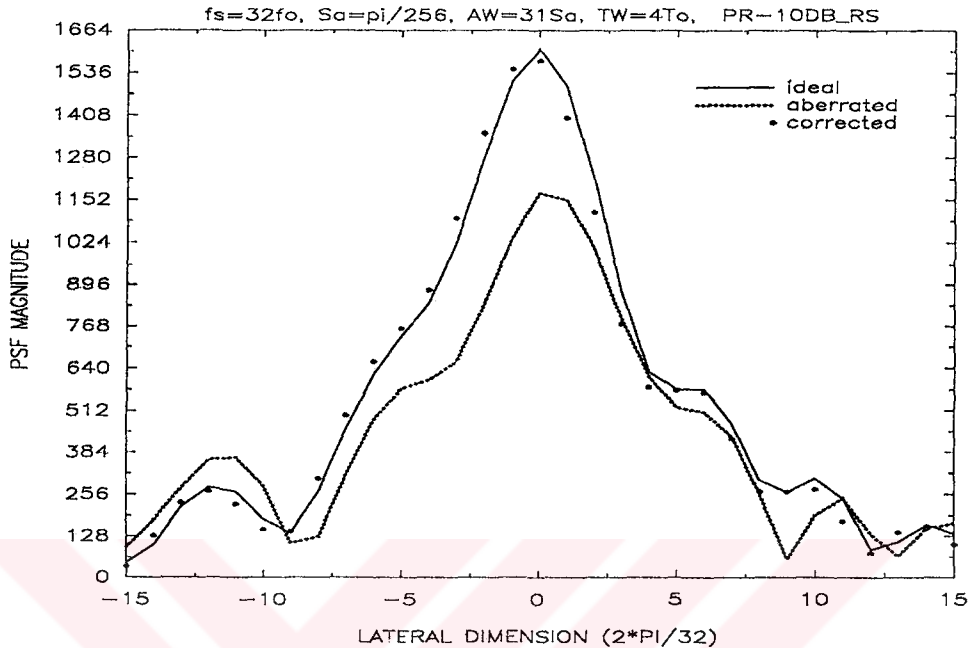


Figure 4.5: Control, aberrated and corrected PSF's.

(Table 4.1). RMS error computations are carried out as follow:

$$RMS\ Error = \sqrt{\frac{1}{N} \sum_{n=1}^N (\tau_n - \tau_n^a)^2} \quad (4.6)$$

where N is the number of array elements, and, τ_n and τ_n^a denote the estimated and the actual aberration delays for n 'th element, respectively.

Simulation results given in Table 4.1 show that the performance of averaged SAD estimator favorably compares to that of 2-D SAD estimator [77]. In addition, the averaged SAD estimator requires a relatively small number of arithmetic operations.

We also perform PSF simulations to examine the phase correction efficiency of the averaged SAD estimator [77]. The reflector distribution consists of a point reflector with -10 dB random scatterers. To obtain a corrected PSF, the estimated aberration delay pattern is employed both in the transmit and receive beamforming. The corrected PSF is compared with the control (non-aberrated) and aberrated PSF's (Fig. 4.5). It is observed from this figure that

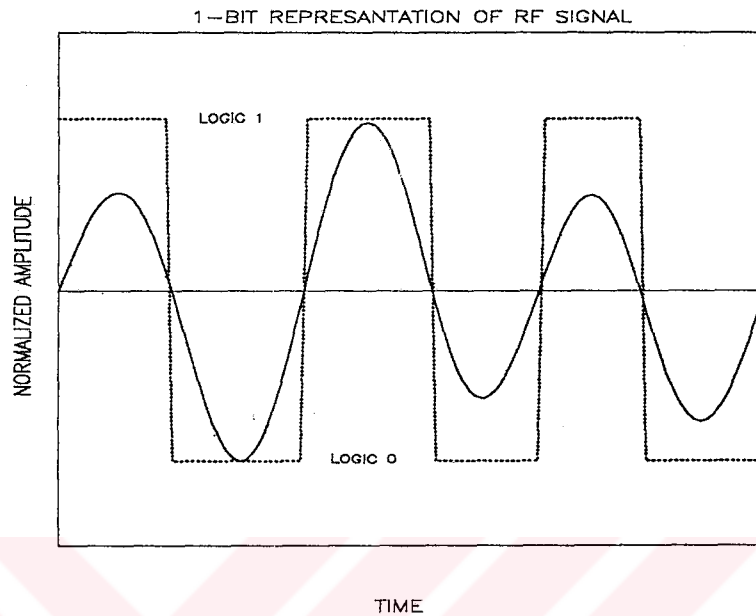


Figure 4.6: One bit representation of the RF signal.

the corrected PSF fits the control PSF very well. Hence, using the averaged SAD phase estimator, the effects of the phase aberration on the array response are eliminated by the phase correction in transmit and receive beamforming. Furthermore, simulations shows that the method is successfully applied for the estimation of aberration pattern in the presence of both point and/or random reflector distributions.

4.2.3 Reduction of Wordlength

Computational efficiency of the SAD technique can be further increased using a shorter word length. The phase information of RF signals can be adequately represented by zero crossings of the carrier [79, 80]. The relative phase difference between two RF signals, then, can be easily detected from shifts in their zero crossings. A single bit word length is sufficient for representation of the zero crossings of the sampled signal. Hence, the SAD technique can be used on RF samples properly quantized to a single bit (Fig. 4.6), where each addition reduces

to a bit level exclusive-or (\oplus). In this case, SAD, $\epsilon'(r_n^i)$, is given by

$$\epsilon'(r_n^i) = \sum_{k=1}^M (\tilde{s}_n^i(k)) \oplus (\tilde{s}_{n-1}^i(k + r_n^i)) \quad (4.7)$$

where $\tilde{s}_n^i(k)$ and $\tilde{s}_{n-1}^i(k)$ are the one bit representations of echo samples $s_n^i(k)$ and $s_{n-1}^i(k)$, respectively. Reduction of the word length to a single bit can cause poor convergence in phase estimation from speckle noise. This effect can be avoided, however, using averaging. No weights are used to further simplify computations.

4.2.4 Performance Analysis

To test the performance of different phase aberration correction techniques, computer simulations are performed using actual RF data sets acquired from a standard graphite-gel AIUM resolution phantom with and without aberrators present. This phantom simulates tissue while providing thin wire reflectors emulating a beacon. The data acquisition scheme and system parameters were outlined in Chapter 3, and were described in detail in [45, 46]. Three data sets were obtained using three plates, made of RTV silicone rubber, placed between the transducer array and the phantom. The first plate has no phase distortion, and is used as a control. The second plate causes phase distortions less than π , whereas the phase distortion imposed by the third plate varies within 2π . In the rest of this paper, we refer to these plates as Plate 0, Plate 1, and Plate 2, respectively.

Portions of the RF data sets are shown in Fig. 4.7 where the wavefronts across the array are depicted for a particular transmit beamforming at a scan angle normal to the array aperture. Phase aberration patterns of the plates are shown in Fig. 4.8. These patterns are estimated from the beacon signals using the full word cross correlation between RF echoes received in adjacent array elements, and represent the “gold-standard”. Image reconstruction and performance evaluation studies are carried out by digitally processing the recorded data, each of about 34 Mega bytes, to emulate the operation of a real-time, digital adaptive imaging system.

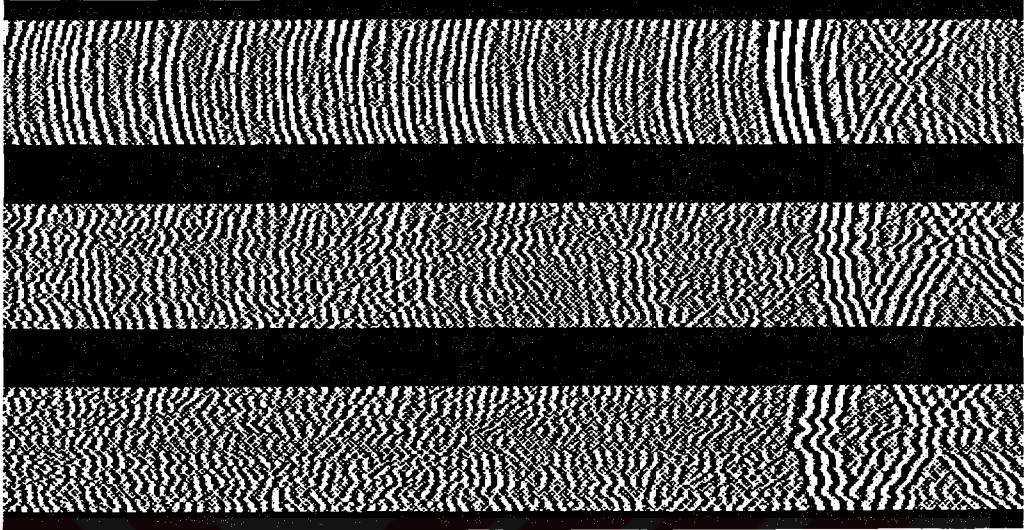


Figure 4.7: Received RF wavefronts across the array for the control and aberrated RF data sets. The first, second and third rows show the portions of data sets associated with Plate 0, Plate 1, and Plate 2, respectively. The vertical and horizontal widths of each row correspond to the aperture size and time interval of 512 samples.

Performance of the SAD method is quantitatively tested and compared with the cross correlation technique [45]. For this purpose, the RMS error between the estimated and the actual aberration patterns are obtained for different parameters affecting the performance of the correction method, such as the number of iterations, the window length used for SAD computation, and the number of scan angles used for averaging [81, 82].

Phase aberration patterns estimated from the beacon signals using full word cross correlation are assumed to be the actual patterns and hence chosen as the gold-standard [46] (Fig. 4.8). All other estimations are based on RF signals from diffuse scatterers. The aberration profile is estimated from scan angles nearly normal to the array face. The transmit focal length is about 80 mm, and the window used for cross correlation and SAD is located 60 mm away from the array. The sampling rate of the RF data sets is increased by 8 times using bandpass interpolation. Hence, phase aberration correction and beamforming operations are performed with about a 142 MHz sampling rate, which corresponds to a phase

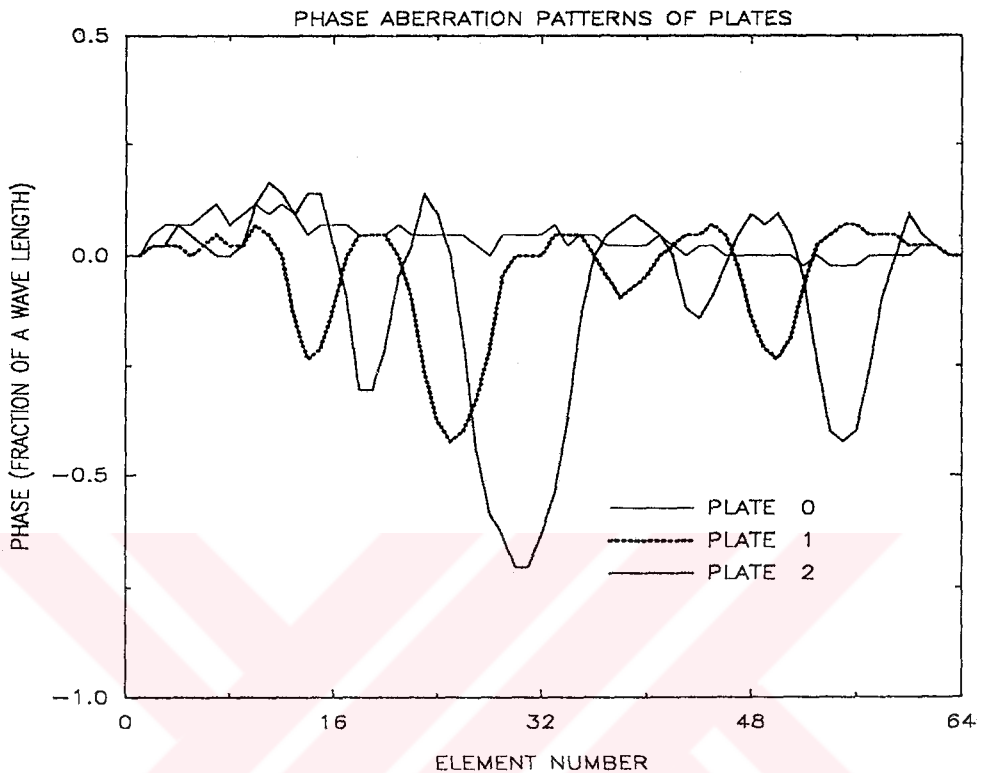


Figure 4.8: Phase aberration patterns of the plates.

accuracy of about $2\pi/43$.

To compare the techniques at different aberration levels, and to investigate their convergence characteristics, the RMS error vs number of iterations was obtained for each data set (see Fig. 4.9, Fig. 4.10, Fig. 4.11). In these figures, five different estimation schemes are presented. The first one uses cross correlation of RF samples between the adjacent channels [45]. The other four correction schemes are applications of SAD with different parameters as indicated in the figures.

The figures show that phase errors can be corrected iteratively. Three iteration cycles are sufficient for reasonably accurate estimation of phase errors. The RMS errors for aberration patterns associated with the Plate 0, Plate 1, and Plate 2 are about 2.5, 4, and 10 percent of a wavelength, respectively. These values

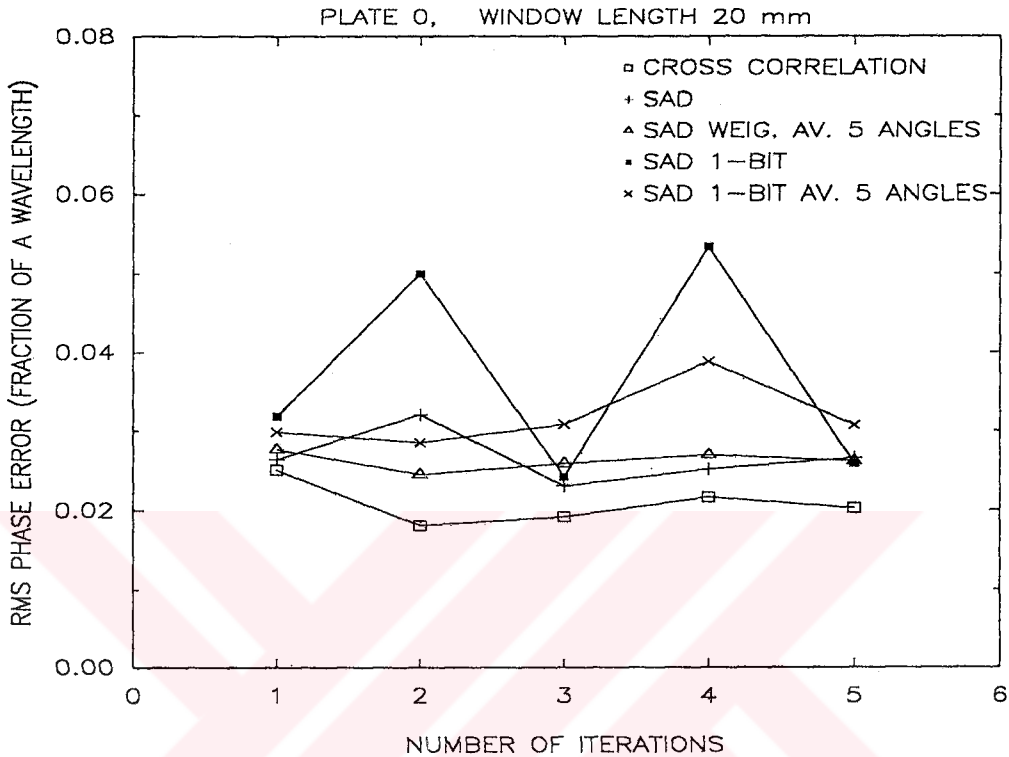


Figure 4.9: Convergence and accuracy performance of phase correction schemes for Plate 0.

correspond to about 1, 2, and 4 units of phase delay (1 unit = $2\pi/43$). The simple SAD minimization with full word has some convergence problems. The SAD with one bit word length is the worst. Averaging, however, eliminates the convergence problem. It should be noted that averaging causes greater phase errors in the first iteration. The full word SAD with weighted averaging shows a better performance compared to other correction schemes. Overall performance of the 1-bit SAD scheme with averaging is comparable to that of the full word cross correlation and full word SAD.

Fig. 4.12 depicts the sensitivity of the phase correction schemes to window size. The figure indicates, as expected, that averaging reduces phase errors. At small window sizes, averaged estimators perform better than cross correlation.

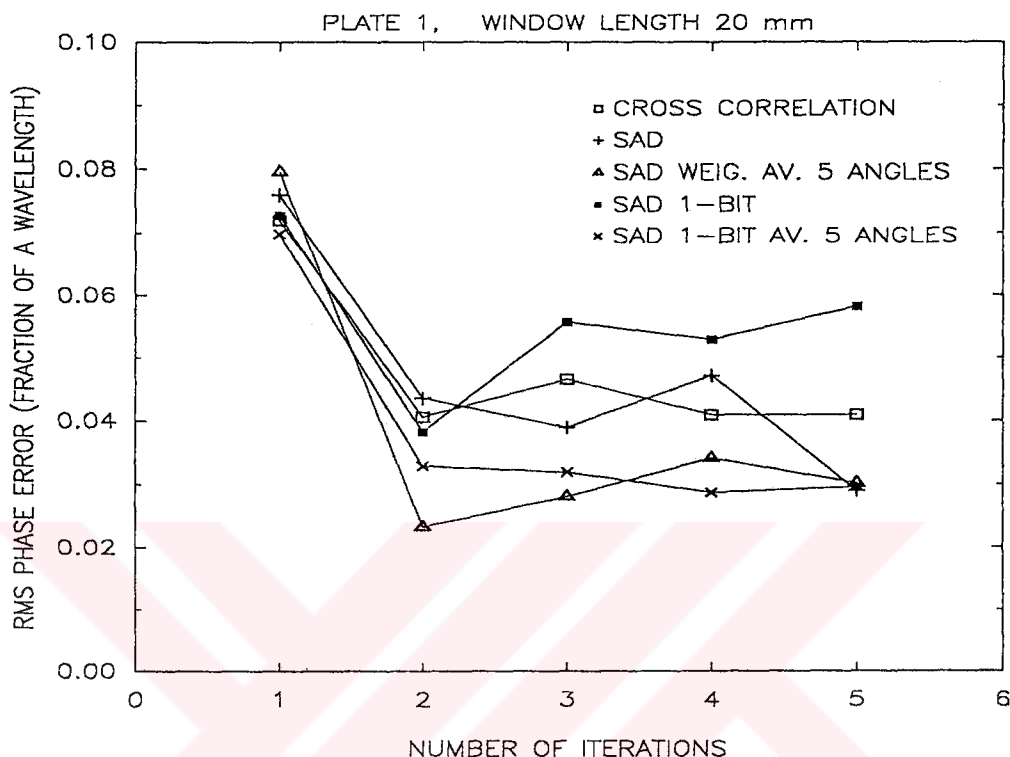


Figure 4.10: Convergence and accuracy performance of phase correction schemes for Plate 1.

It is also observed that the use of one bit wordlength does not necessitate to an increased window size relative to the other schemes.

Proper selection of the number of angles for averaging is critical. It must be large enough to get a stable estimate in a few iterations. On the other hand, it must be small enough to confine the region to the vicinity of particular reflecting structures and avoid the effects of other scatterers. To choose a proper value, the full word SAD with weighted averaging and 1-bit SAD with simple averaging are tested for different numbers of scan angles (see Fig. 4.13). It is observed from these figures that averaging over five scan angles is a proper choice for both schemes.

To test overall image quality, images of a section of the phantom are

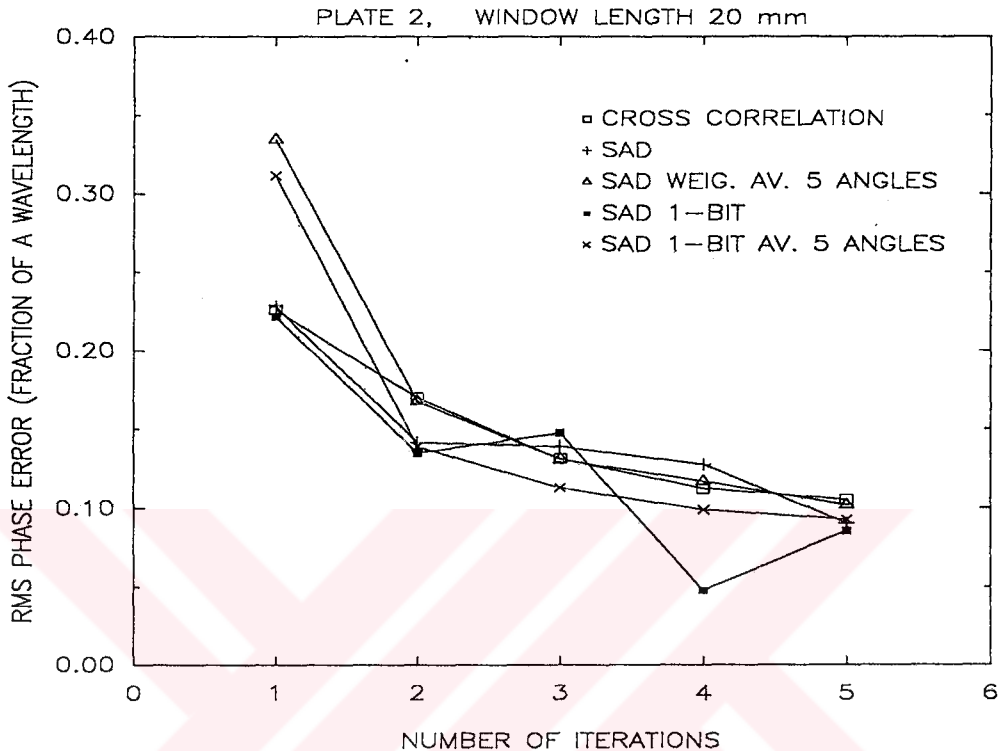


Figure 4.11: Convergence and accuracy performance of phase correction schemes for Plate 2.

reconstructed using both cross correlation and SAD correction schemes. Fig. 4.14 depicts the control, aberrated and the corrected images displayed on a purely logarithmic scale over a 50 dB dynamic range. For each corrected image, the phase aberration pattern used in correction is estimated in three iterations from diffuse scatterers over scan angles nearly normal to the aperture face. The window length used for cross correlation and SAD are 20 mm. It is observed from the images shown in Fig. 4.14 that the performance of the full word SAD with weighted averaging of estimates over five scan angles, compares favorably to that of the cross correlation method. In addition, image quality of the SAD with one bit wordlength and averaging of estimates over five scan angles, is as good as full word SAD and full word cross correlation.

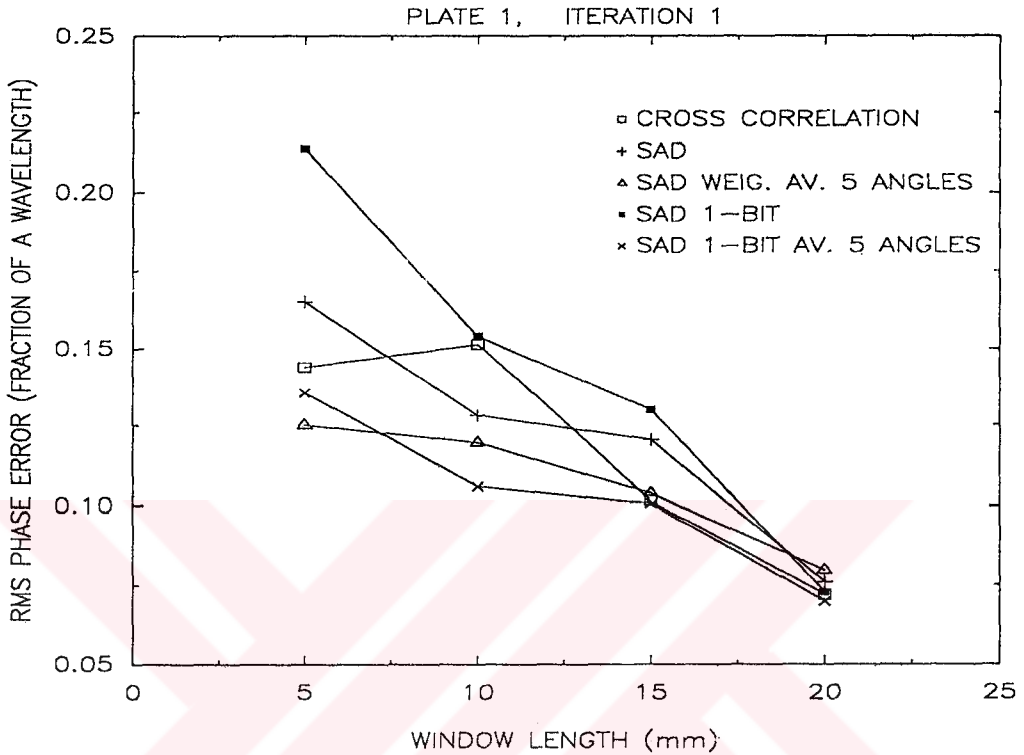


Figure 4.12: Effect of window size on the accuracy of phase estimation techniques for Plate 1.

Comparison of the control image with its corrected versions indicates that no artificial distortion is generated. However, it is observed that corrected versions of aberrated images are not the same as the control image. This is because the RTV plates also produce amplitude distortions across the array, in addition to simple phase aberrations [46] (Fig. 4.15). Amplitude variations degrade beam quality, and limit the accuracy of phase estimation. Furthermore, aberration correction even with perfect phase compensation can not produce an image which is an exact replica of the control image due to amplitude distortions.

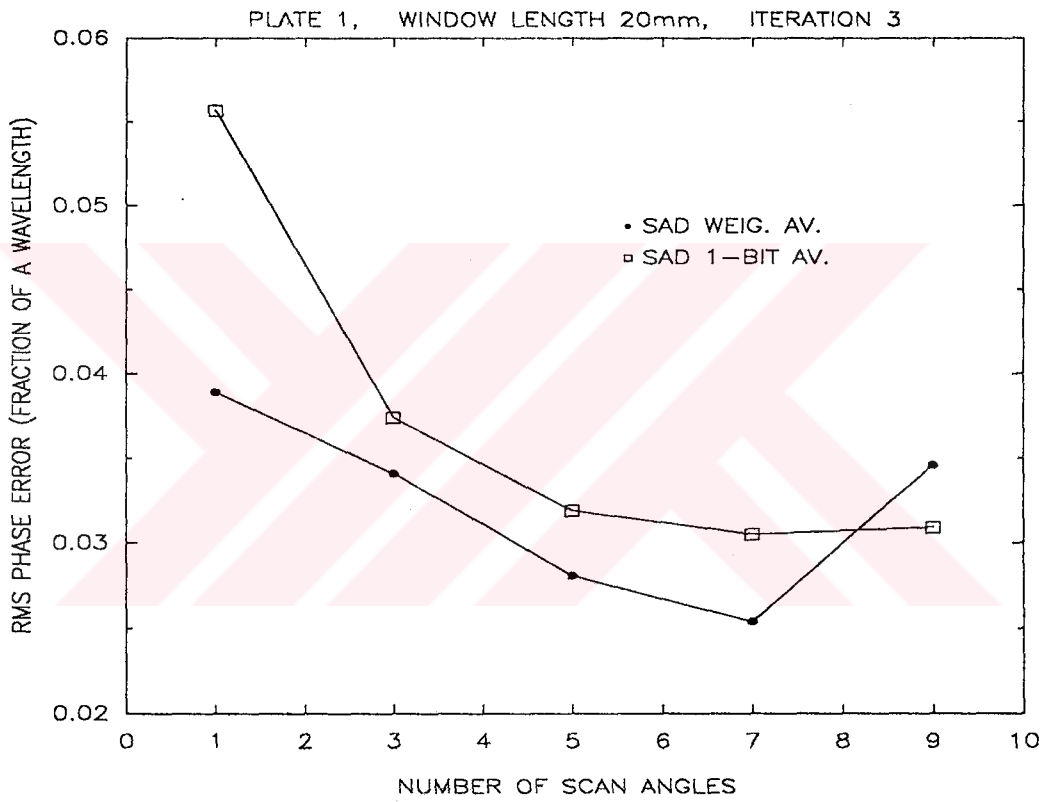


Figure 4.13: Effect of the number of scan angles used for the averaging of phase estimates on the accuracy performance the SAD with full word and one bit word length.

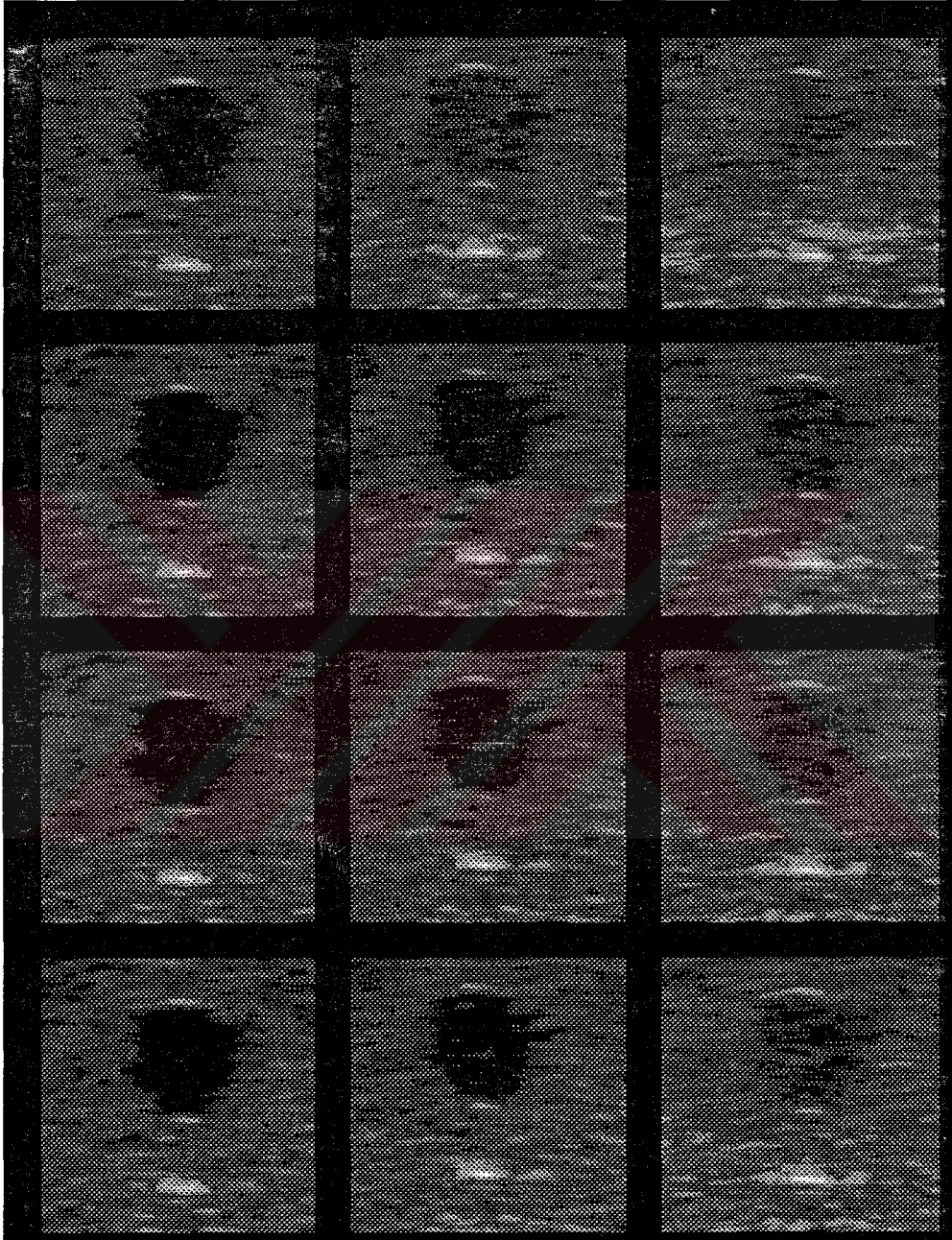


Figure 4.14: Images of a section of the phantom. Control and aberrated images (row 1). The corrected images using full word cross correlation (row 2), full word SAD with weighted average of phase estimates over five scan angles (row 3), and SAD with one bit word length and average of phase estimates over five scan angles (row 4). The images in the first, second and third columns correspond to the data sets associated with Plate 0, Plate 1, and Plate 2, respectively.

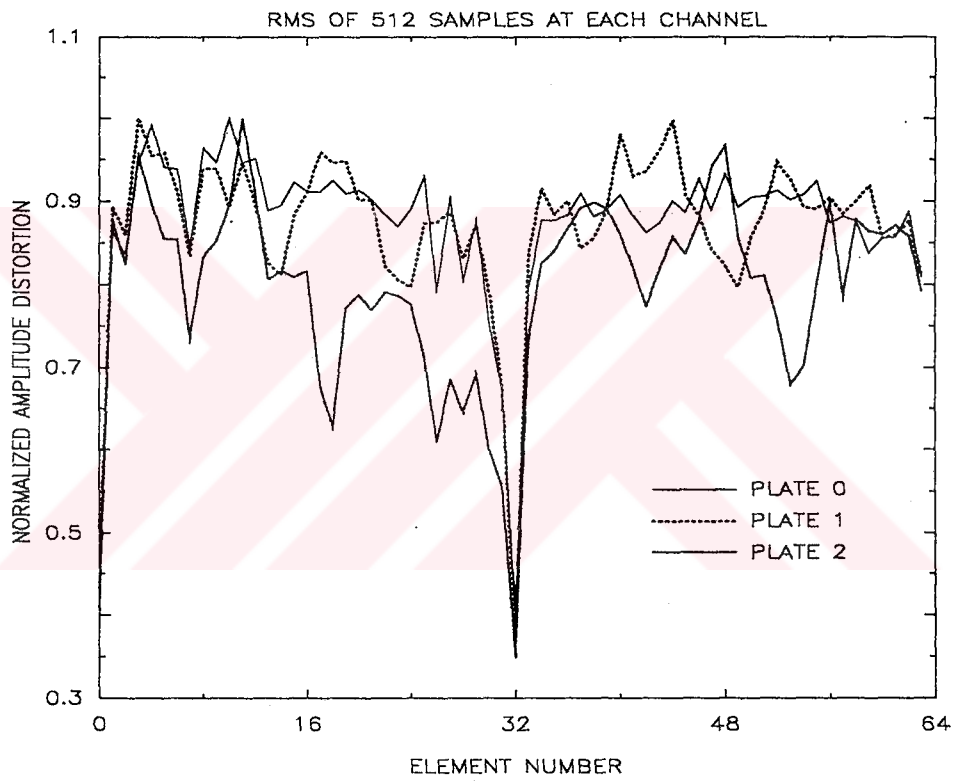


Figure 4.15: Amplitude distortions of the plates across the array.

4.3 VLSI Architectures for Phase Estimation

4.3.1 Fullword SAD

Hardware realization of the phase aberration detection using full word SAD technique, requires delay elements and processing units for computation of the SAD terms for the sample vectors with different shift indexes. The shift index of the minimum of the SAD's corresponds to the time shift between the two channels.

Pipelined architecture developed for full word SAD is shown in Fig. 4.16. In this structure, the samples in the SAD window are piped in as inputs A and B . In order to provide shifted data, one of the inputs, A , is delayed through the pipelined delay elements. The number of stages of SAD and delay units are K and $K - 1$, respectively. The samples pairs are then accumulated in SAD units. When the last sample pair in the SAD window is processed in the SAD unit, they are sent out to the comparator which outputs the minimum of its two inputs and the corresponding shift index. Thus, the process is repeated in the pipelined stages, and at the output of the last stage, the minimum of the SAD's and its index are obtained.

The structure shown in Fig. 4.16 is cascadable for larger shift indexes. The speed of this network is determined by the slowest of an absolute difference operation and a comparison used for selection of the minimum of two SAD terms. The throughput will be proportional with this speed and inversely proportional with length of SAD window

4.3.2 One Bit SAD

A processing unit consisting of three pipelined stages is developed (see Fig. 4.17) to form a flexible 1-bit SAD architecture by simply cascading a number of these units [52].

In the processing unit shown in Fig. 4.17, the binary data vectors in the SAD window, $(\{a_m\}_{m=1}^W$ and $\{b_m\}_{m=1}^W$ in Eq.. 4.7) are serially entered to the unit, from

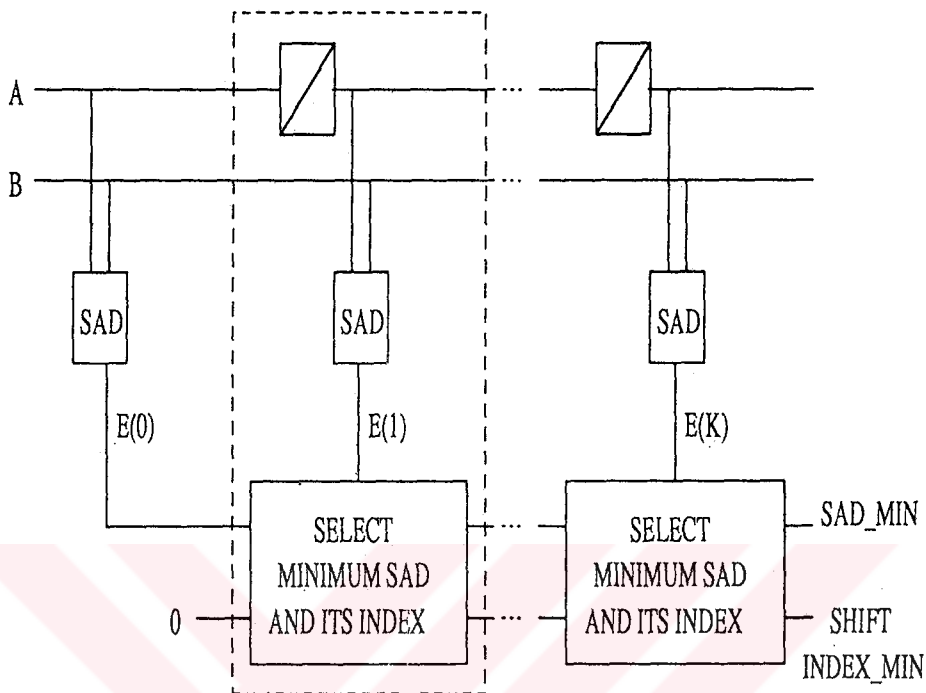


Figure 4.16: Full word SAD architecture.

inputs A and B . The unit also takes a binary reset input, R , and cumulative data inputs, SAD_MIN , SI_MIN , and SI . These are the minimum of SAD terms, the shift index corresponding to the minimum SAD, and the shift index indicating the shift count of the previous unit, respectively. The shift index is incremented and sent out to the succeeding unit. At any time, the shift index of the unit is regenerated. The computation of the SAD term corresponding to a different shift index is carried out using a counter which is updated by the result of XOR of the binary inputs. The counter is an upcounter which increments its value, if the XOR of the inputs is 1. When the last data inputs are processed, then the output of the counter becomes the result of the SAD of all binary data within the window. This is compared with the SAD_MIN , and the smaller one and its corresponding index are sent out.

The unit outlined above, computes the SAD term, $\epsilon(k)$, and then compares it with the input $SAD_MIN = \min.\{\epsilon(k-1), \epsilon(k-2), \dots, \epsilon(0)\}$. It outputs the the minimum of the SAD terms, $\{\epsilon(k), \epsilon(k-1), \dots, \epsilon(0)\}$, and corresponding index.

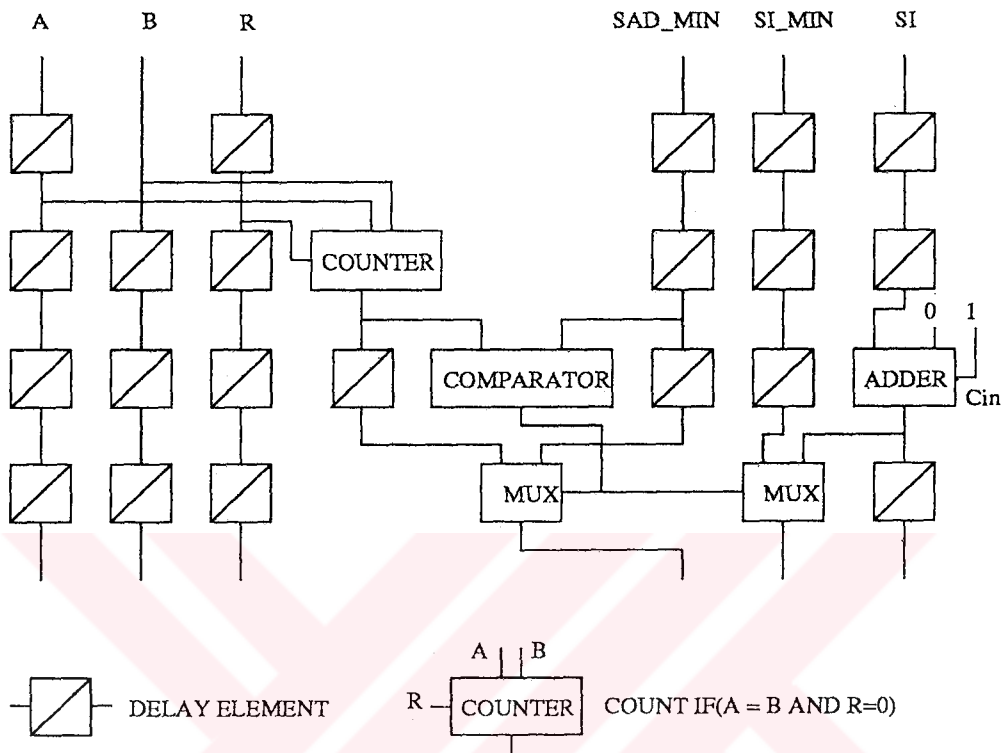


Figure 4.17: Processing unit for the 1-bit SAD architecture.

One can cascade K stages of the unit to form a SAD network of K shift indexes. Therefore, the minimum of K SAD terms and associated indexes are computed in a pipelined manner and become available at the output the last unit. The maximum number of the cascaded stages (i.e., the maximum value of shift index, SI , which equals to K), is determined by the size of the adder used for updating shift index, whereas the maximum number of input data (i.e., the length of the SAD window, W) is determined by the counter size.

The proposed 1-bit SAD hardware structure can be modified to increase the throughput further. This can be achieved in a systolic scheme by employing bit level pipelining and parallelism [83, 84]. Such an architecture with very high throughput is depicted in Fig. 4.18. In this architecture, the binary data, $\{a_m\}_{m=1}^W$ and $\{b_{m+k}\}_{m=1}^W$ are applied to the inputs in parallel. There are three bit-level processing elements: delay, half adder, and XOR elements. Since all

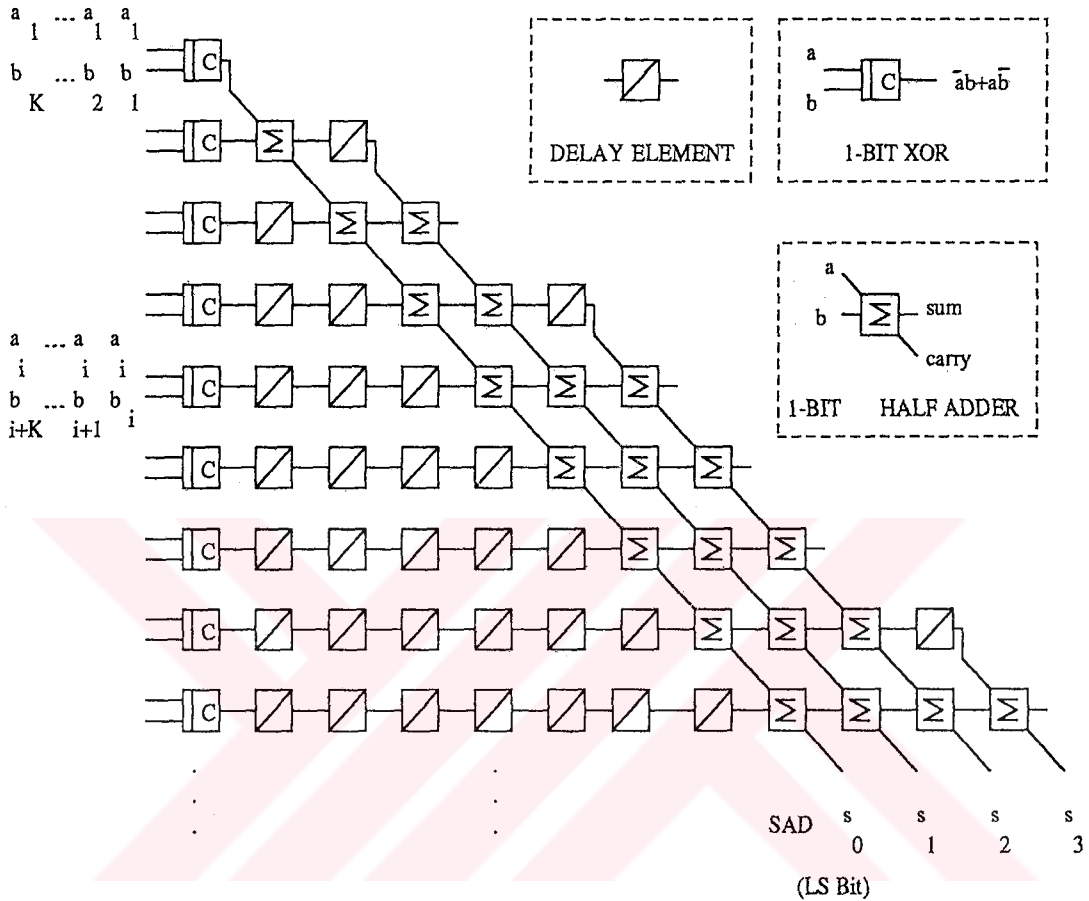


Figure 4.18: The high throughput architecture for 1-bit SAD.

operations are pipelined at bit-level, the computation time of a SAD term is determined by a bitwise XOR operation. All of the SAD terms, $\{e(i)\}_{i=1}^K$, are computed at K pipelined clocks. The minimum of the SAD terms can be found using a fast comparator or a sorter [85, 86].

VLSI design complexity of the architecture given in Fig. 4.18 is very low. Since the area of the architecture increases with $W^2/2$, it is suitable for the realizations with a reasonably large W

4.4 Concluding Remarks

A new phase aberration correction scheme based on SAD is presented for phased array ultrasound imaging. The performance of the proposed method is investigated using the experimental data. The method can be used for estimation of the aberration pattern from echo signals reflected by line targets and/or diffuse scatterers. Computational complexity of the SAD method is relatively low since it involves only additions, and the overhead due to the averaging is insignificant. The computational efficiency is further improved using a single bit word length. Dead elements in the array decrease the accuracy of phase estimation using SAD minimization, and the degradation in the estimation performance is similar to that for cross correlation [65].

VLSI architectures for the phase estimation via SAD minimization with full word and one bit are developed. In addition, a high throughput architecture is proposed for angle and range dependent phase correction applications. Each of these architectures is regular and modular, and hence offers an easy and straightforward implementation.

Chapter 5

VLSI Circuits

5.1 Implementation

The proposed hardware structures for the interpolator, beamformer and phase estimator are implemented in 1.5 μm n-well double metal CMOS technology of IMEC-MIETEC of Belgium, using full-custom VLSI design techniques. Due to the pipelined structure and systolic data flow, a sequential circuit design is employed with two phase nonoverlapping clocking strategy: the inputs are latched in during the first clock, and the computed outputs are sent out during the second clock. The circuits can function correctly even if the complement of the first clock is used as the second clock, but the operations of the circuits with two nonoverlapping clocks are more reliable. In design of the circuits, the standard (complementary) CMOS logic style because this logic style offers a more reliable timing and an easy mapping in layout compared to the other logic styles. Furthermore, its area and speed performance is comparable with the other styles [87, 88].

In layout generation step, firstly, the floor plans of the chips are completed. Layouts of the networks are edited hierarchically starting from the basic cells. Then circuit equivalents of the layouts are extracted and simulated. For editing and simulations, we have used the Berkeley CAD Tools of University of California [89] and VLSI Tools of University of Washington [90] running under the *Unix*

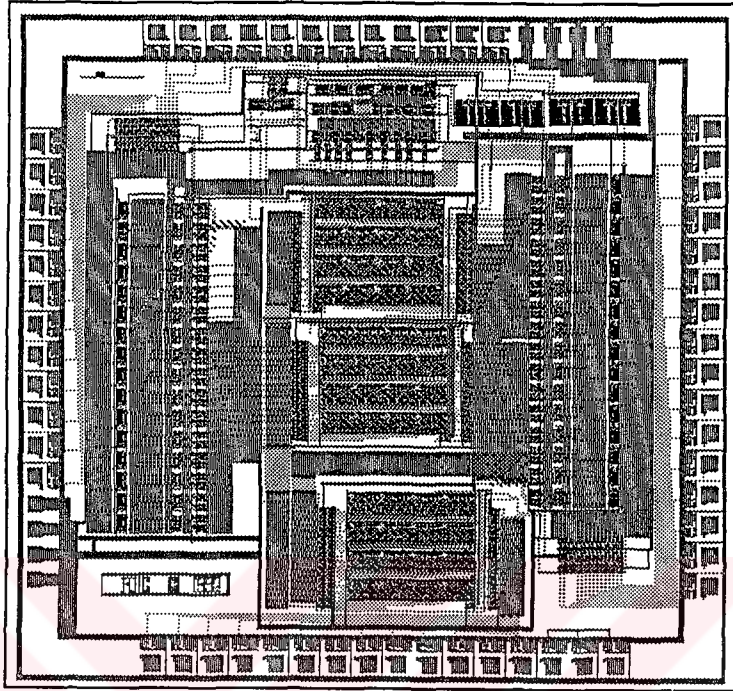


Figure 5.1: Layout of the designed interpolator chip.

operating system on a *SUN Sparc* workstation. Layouts are edited with the Magic. The timing and logic simulations are performed by using the Hspice, Rn1, and Irsim circuit simulation tools.

The testing of the designed circuits are easily accomplished by the functional test techniques, since the operations of the units are selectively probed by issuing proper test vectors [91].

5.2 Interpolator

The linear interpolator structure shown in Fig. 5.1 is implemented as a single chip (see Fig 5.1 and Table 5.1). Each of the input samples and the interpolated output sample is 16-bits, whereas the T_1 input is 3-bits. The throughput of the chip is 40 Mega interpolations/s, which can meet the speed requirements of adaptive beamforming applications.

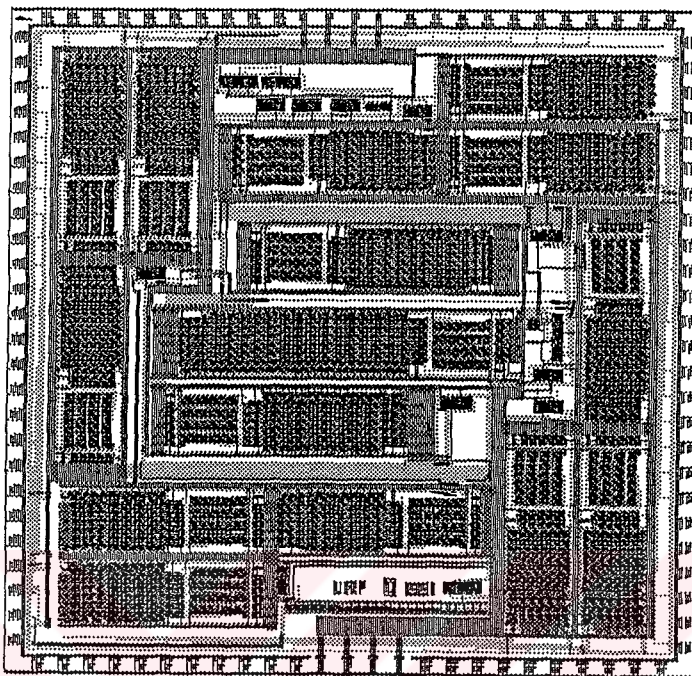


Figure 5.2: Layout of the designed beamformer chip.

5.3 Beamformer

A receive beamformer for $N = 16$ is realized by connecting 15 processing units in an inverse binary tree structure to form the core of the chip (see Fig 5.2 and Table 5.1). The chip consists of the lowest four stages of the network for $N = 256$, outlined by a dashed rectangle in Fig. 3.10. Since the lowest four stages have the longest FIFO's, one can connect a number of the chips to form a network for $N \leq 256$ (Fig. 5.3). Maximum throughput of the chip is 40 Mega-beamforming-operations/s. The chip has 16 multiplexed inputs and one one multiplexed output, 16-bits plus one status bit each. Overall result of coherent addition is truncated to 16-bits from 20-bits, while the maximum dynamic range requirement is about 12 bits.

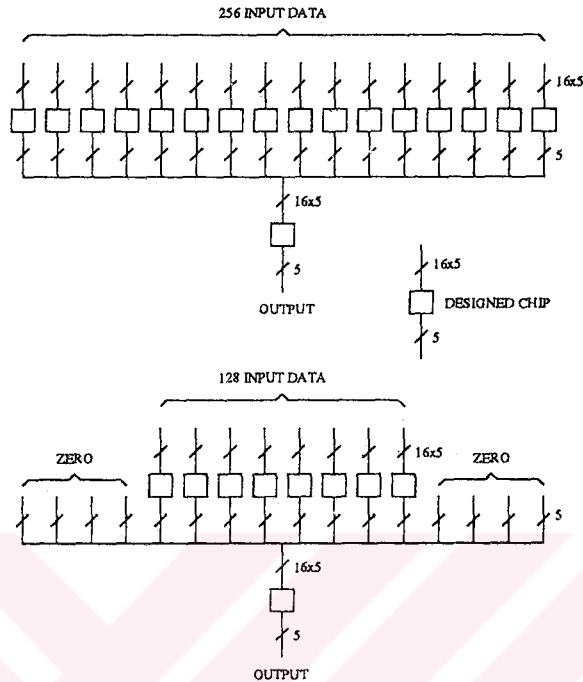


Figure 5.3: Connections of the beamformer chips for 256 and 128 channels.

5.4 Phase Estimator

A phase aberration estimation chip, consisting of 8 cascaded units depicted in Fig. 4.17, is implemented (see Fig 5.4 and Table 5.1). The word lengths are chosen sufficiently long to offer the chip to be used for sufficiently large window sizes and to be cascaded for larger shift indexes. The single chip can be used for window sizes up to 4096 samples with 8 shift indexes, whereas for shift indexes up to 128, the number of chips to be cascaded is the smallest greater integer of $K/8$. For the applications requiring cascaded connections, the pipelined data flow scheme of the chip is depicted in Fig 5.5 A single chip can be used in phase aberration detection, where the shift index of adjacent array element pairs does not exceed 8 for sampling rates up to $50f_o$, and for phase aberration variation within a cycle. On the other hand, the window size is sufficiently long for phase aberration correction from both point reflectors and the diffuse scatterers for sampling rates up to $50f_o$. As an example, the SAD window of size 4096 corresponds to about

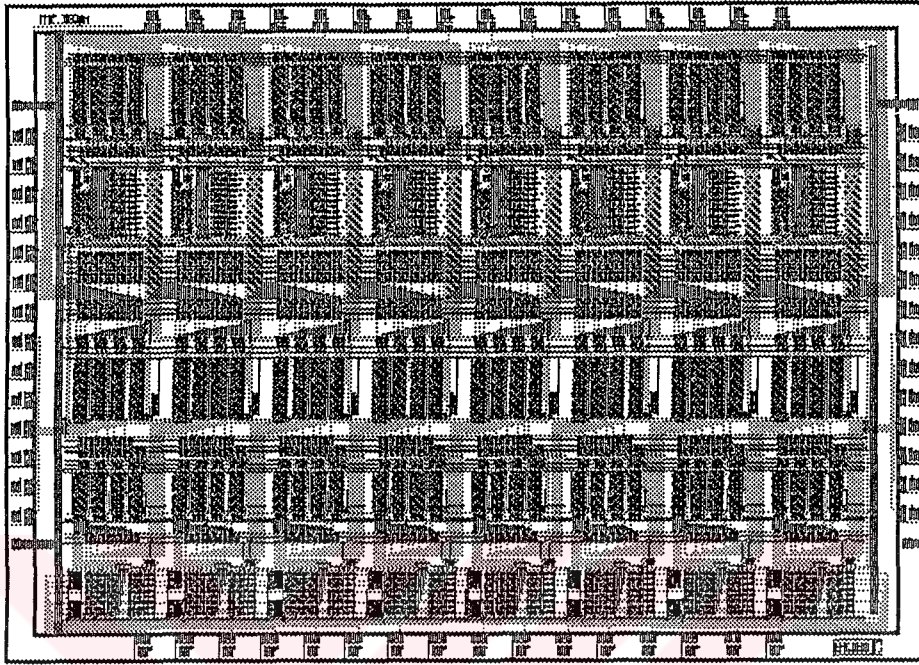


Figure 5.4: Layout of the designed 1-bit SAD chip.

20 mm for $f_o = 3.33$ MHz and sampling rate of $43f_o$, which are the parameters used in the phase aberration correction of the images shown in Fig. 4.14.

The computation at each pipelined stage is completed in about 20 nsec resulting in a pipelined speed of 50 Mega operations/s. Thus, the throughput of the chip is about $50/W$ Mega outputs/s. This enables the phase aberration detection of about 12 K/s with $W = 4096$. In sector imaging, the phase aberration correction can be applied at each frame where the phase correction iterations can be carried out on the consecutive frames. Also, the angle dependent correction can be carried out for a number of scan angle groups on each frame. For 128 scan angles/frame and 30 frames/s, the number of the phase aberration correction operations is 3840. Hence, the speed of the designed chip is adequate for phase aberration correction at each scan angle for every frame.

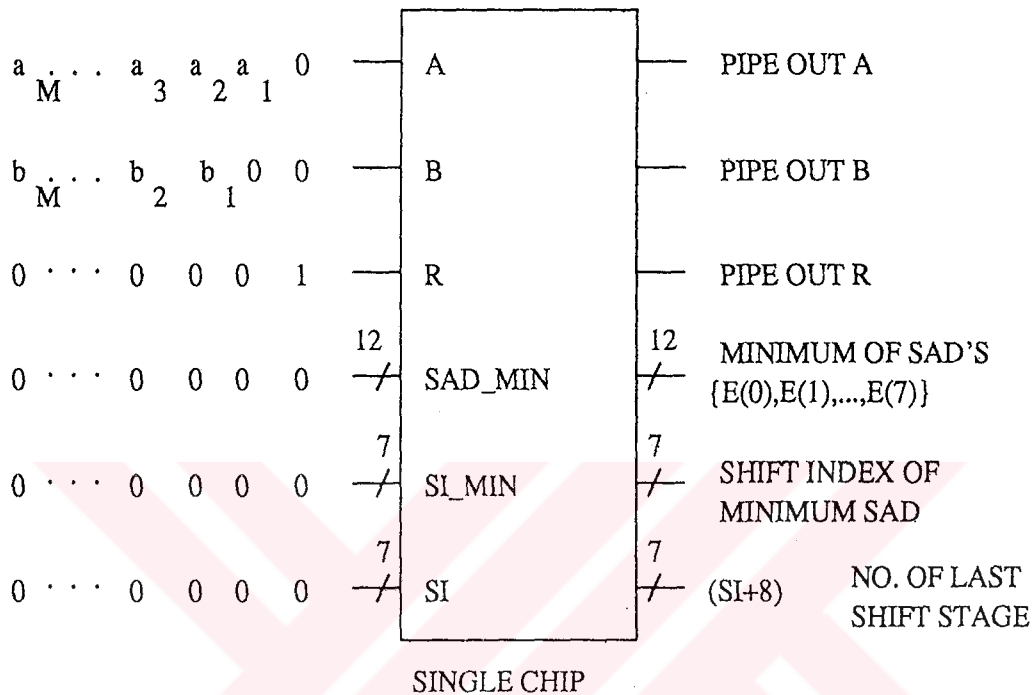


Figure 5.5: Pipelined data flow scheme of the 1-bit SAD chip.

Parameter	Interpolator	Phase Estimator	Beamformer
Die size (mm ²)	2.8 × 3.0	4.4 × 6.0	6.6 × 6.7
Transistor count (K)	5	28	40
Pin count	64	64	100
Max. clock freq. (MHz)	40	50	40
Max. throughput (Mega outputs/s)	40	50/W	40

Table 5.1: Characteristic parameters of the designed chips.

5.5 Concluding Remarks

The VLSI chips presented here have not been fabricated. Their characteristic parameters given in Table 5.1 are estimated through the simulations to depict the VLSI feasibility of architectures.

Proposed VLSI circuits can be used to form a fully digital front-end hardware for phased array ultrasonic imaging. They offer flexibilities in different system parameters such as channel counts, window sizes, and scanning format. The chips properly meet the interconnection and data flow scheme employed in the front-end architecture shown in Fig. 3.1 of Chapter 3, and hence can be easily configured in such a scheme. For the applications with channel count larger than 16, the connection diagram for the beamformer chips shown in Fig. 5.3 must be considered.

Chapter 6

Results and Conclusions

Computationally efficient digital beamforming techniques for reduction of delay quantization errors, receive focusing, and for phase aberration correction are presented. Performances of these techniques are tested and illustrated using the experimental ultrasound phased array RF data sets acquired from a tissue-mimicking phantom. Special purpose VLSI circuits based on these techniques are proposed. Single-chip realizations of the circuits using full-custom CMOS VLSI design techniques are outlined.

To increase the timing accuracy in delay and sum based beamforming and in phase aberration correction, a simple bandpass upsampling scheme seems to be a cost-effective solution. Designed VLSI upsampling circuit based on the linear interpolation with coefficients in discrete powers-of-two space can meet the speed requirements of the real-time adaptive beamforming.

Phased array ultrasound image reconstruction by employing receive beamforming at the raster sample points instead of the radial points reasonably improves the image quality and completely eliminates the scan-conversion process, at the expense of increased beamforming operations. This overhead can be solved by the proposed VLSI receive beamforming scheme which possesses following features: i) small storage for data synchronization, ii) flexibility in applications with different number of array elements, iii) operating capability at real-time rate, and iv) feasibility for custom chip(s) implementation. VLSI

implementation for large N is not very feasible because of the large chip area and large number of I/O's. The modularity of the structure can be employed effectively, however, by proper choice of FIFO sizes, and by using the beamformer chips with $N = 16$. Furthermore, the designed beamformer circuit can perform real-time receive beamforming at the radial or raster focal points.

To obtain the accuracy bounds of time delay estimation through minimization of SAD, it is not easy to follow an analytical approach due to the non-linear nature of SAD. Such an analysis may be performed by imposing some assumptions which can not be met in practice, and hence the results can not depict relevant information for aberration correction performance, because of the practical limitations on the accuracy, such as delay quantization. Therefore, the SAD performance is investigated through the simulations using numerical and experimental data. Numerical simulations, employing the practical aberration correction parameters (see Appendix B), depict that the mean and standard deviation of the time delay estimate using SAD are zero and one half of delay quantization level, and are approximately the same as that for correlation.

Further analysis of the SAD phase estimators indicate that 1) reduction of wordlength to a single bit decreases the stability in iterations, and 2) averaging of phase estimates over a number of scan angles increases the accuracy and stability of estimation in iterations. The stability in phase correction is a critical issue since different phasing in successive iterations produce different images that confuses clinicians. A general result of the analysis is that the phase correction can be achieved by employing a simple phase estimator. Hence it is concluded that the phase estimation using SAD minimization with a single bit word length and averaging estimated phase patterns over a number of scan angles compares favorably to computationally more complex methods, whereas it lends itself to real-time implementation through a simple architecture

The hardware structures developed for phase estimation using full word and 1-bit SAD schemes have very low VLSI design complexities and offer flexibilities in shift-index and SAD window sizes. The designed phase estimator chip based on the 1-bit SAD can meet the speed requirements of one and two dimensional

angle dependent, real-time phase aberration correction applications. Should a faster phase error estimation be required, such as for correction of both angle and range dependent phase errors, the proposed 1-bit SAD hardware structure (Fig. 4.18) with very high throughput can be employed. However, it is suitable for the realizations with a reasonably large window used of computation of the SAD, since the area of the architecture is proportional to the square of window size.

In the digital front-end hardware as depicted in Fig. 3.1, the processing units can be realized using the designed chips (interpolator, phase estimator, and beamformer). The upsampling on each channel can be performed using an interpolator. The phase aberration estimation on the channel pairs can be realized by the phase estimator. Both the resampling and the beamforming operations can be handled by the beamformer chip(s), where the input status entry controls the sample selection. For an N channel phased array imaging system, the number of chips for upsampling, phase estimation, and beamforming are N , $N - 1$, and smallest greater integer of $N/16$, respectively.

The proposed front-end circuits involve sampling of RF echo signals received from all array channels. This is a major limitation in all digital beamforming schemes as well as the one discussed in this work. The speed of the ADC's, however, is not critical, since a special interpolation circuit is also employed to decrease the effects of delay quantization.

In an attempt to increase the efficiency of front-end hardware scheme, one may consider to integrate the ADC units with the associated beamforming electronics for two or a sub-group of array elements into a single VLSI circuit [92]. Examination of this possibility with present integrated circuit technology did not give the desired result. A serious cross-talk problem due to the mixed analog and digital circuits, and high cost of the VLSI chip because of the very large area, have been encountered [93].

In phased array ultrasonic imaging, the achievement of higher resolution necessitates the use of increasing channel counts with two dimensional array geometries [94, 95, 96]. In many applications, however, image quality is

significantly degraded by phase aberrations, and hence resolution may not be improved significantly with large arrays unless adaptive beamforming techniques are employed. Therefore, phase aberration correction in imaging with large arrays is more critical than with small sized arrays [97]. Use of two dimensional arrays involves two dimensional phase aberration correction [66, 65, 67, 98]. The proposed SAD phase aberration correction schemes can be also applied in two dimensional phase correction while maintaining its low computational complexity, which involves further study.

Large numbers of inoperable array elements are encountered in imaging with large aperture arrays due to the discontinuous acoustic window into the body [65, 99, 58]. Also, RF data on a channel can be degraded due to elements being blocked by air, by fabrication errors in the array, by connector wires breaking or by problems in the electronic circuitry. Performance of the aberration correction based on the time delay estimation on RF signals critically depends on the spatial covariance measured across the array, especially in the presence of dead elements. The estimation accuracy decreases as the covariance decreases. The van Cittert-Zernike theorem applied to the pulse-echo ultrasound implies that the spatial covariance measured by correlation is linear across the array [100]. The proposed phase correction technique based on the time delay estimation through SAD minimization necessitates the measurement of spatial covariance across the array by employing SAD as the covariance measure. The preliminary measurements using the experimental data (see Appendix C) indicate that the spatial covariance across the array measured by correlation and SAD are not the same, but their sensitivity to focusing and aberration are comparable. The measurements also indicate that the effect of the reduction of wordlength to a single bit in SAD computation, is insignificant. Furthermore, it is observed from the figures given in Appendix C that the proposed SAD phase aberration correction schemes can be used for phase correction in the presence of inoperable elements upto about 10 % of overall array elements. Analysis and compensation of the effects of missing elements in array response and in phase estimation using SAD are other issues requiring further work.

The front-end hardware architecture discussed in Chapter 3, employs the time delay and sum operations for beamforming. Alternative front-end schemes involving beamforming with course time delays followed by fine phase adjustment and sum operations, have been also used [92, 23]. The phase delays can be accurately realized by the phase rotation techniques, and the sampling rate of the ADC's can be kept at the Nyquist rate of RF signal. The phase rotation, however, introduces phase error because it can be adjusted correctly to only a single frequency component in the RF band, which is chosen to be the carrier frequency. This drawback can be eliminated by employing parallel phase rotation on the RF subbands for each array channel. To lead the future work, a beamforming scheme based on this approach is outlined and discussed in Appendix D. Integration of the phase estimation, which necessitates high sampling rate, into phase rotation based beamforming schemes is subject for the future work.

Target-detection capability of phased array ultrasonic images is severely degraded by the presence of speckle which is an interference pattern produced by scattering from unresolvable random structures [101, 102, 103]. The proposed adaptive digital front-end architecture can be extended further for integration of an adaptive speckle reduction scheme involving linear and/or non-linear signal processing based on statistics of RF data and speckle [104, 105].

Appendix A

Sensitivity of SAD to Phase

This appendix covers the derivations to show that the SAD of two RF signals is a direct measure of their relative phase difference, for both the point reflector and random scatterers.

For the sake of simplicity, the derivations are carried out in continuous time domain where the SAD can be viewed as the error which is a function of the delay. It can be defined as the integral difference of two RF echo signals over a time window:

$$\epsilon(\tau_e) = \int |s_n(t) - s_{n-1}(t + \tau_e)| dt \quad (\text{A.1})$$

where the $s_i(t)$ is the echo signal received from the i 'th array element. In the following sections, it is shown that the time offset, τ_e , which minimizes the above error measure is the relative time shift, i.e., relative phase between the two channel signals.

A. Point Reflector

Assume that the pulse is sufficiently long so that continuous wave approximation is valid, and also assume that the element factor is unity, then the transmitted beam from a phased array can be written as

$$B(r, \theta) = \sum_{n=1}^N a(x_n) e^{-j\omega_0 t_n(r, \theta)} \quad (\text{A.2})$$

where the time variation is suppressed. The aberrated apodization window function, $a(x)$, is given by

$$a(x) = a_0(x)e^{j\phi_a(x)} \quad (\text{A.3})$$

where $a_0(x)$ is the nonaberrated apodization window function, and $\phi_a(x)$ is the phase function of the aberration pattern. When the above beam is transmitted, the received signal from the i 'th element becomes

$$s(x_i) = a(x_i) \int dr \int d\theta B(r, \theta) R(r, \theta) e^{-j\omega_0 t_i(r, \theta)} \quad (\text{A.4})$$

For a point reflector located at (r_0, θ_0) , the reflectivity function becomes $R(r, \theta) = \delta(r - r_0, \theta - \theta_0)$. Then the signal of the i 'th element received from the point target is given by

$$s(x_i) = a(x_i) B(r_0, \theta_0) e^{-j\omega_0 t_i(r_0, \theta_0)} \quad (\text{A.5})$$

Here, the error measure can be written as

$$\epsilon(\phi_e) = |s(x_n) - s(x_k)e^{j\phi_e}| \quad (\text{A.6})$$

In order to show that the error expression is a measure of the relative aberration of the n 'th and k 'th elements, one can rewrite the error expression as

$$\epsilon(\phi_e) = |B(r_0, \theta_0)| |w_0(x_n)e^{j\omega_0 t_n} e^{j\phi_a(x_n)} - w_0(x_k)e^{j\omega_0 t_k} e^{j\phi_a(x_k)} e^{j\phi_e}| \quad (\text{A.7})$$

where t_i is used for $t_i(r_0, \theta_0)$. If we assume that apodization function is uniform, $w_0(x) = 1$, then we can write

$$\epsilon(\phi_e) = 2 |B(r_0, \theta_0)| \left| \sin\left(\frac{1}{2}\{\omega_0(t_n - t_k) + \phi_a(x_n) - \phi_a(x_k) - \phi_e\}\right) \right| \quad (\text{A.8})$$

Note that $|B(r_0, \theta_0)|$ is the value of the transmitted beam from the aberrated array, at the point reflector location. Using the ϕ_e as the minimizing parameter, and assuming that the relative phase variation is not larger than 2π , then the minimum of this expression occurs at

$$\phi_e = \omega_0(t_n - t_k) + \phi_a(x_n) - \phi_a(x_k) \quad (\text{A.9})$$

The first term in this expression is the focusing phase whereas the difference of the last two terms corresponds to the relative phase aberration. Thus, the error function is a measure of the relative phase difference between two RF signals received from adjacent array elements.

B. Random Scatterers

Using Eq. A.4 and Eq. A.6, the error measure is written as

$$\epsilon = \left| \int dr \int d\theta B(r, \theta) R(r, \theta) \{ a(x_n) e^{-j\omega_0 t_n(r, \theta)} - a(x_k) e^{-j\omega_0 t_k(r, \theta)} e^{j\phi_e} \} \right| \quad (\text{A.10})$$

$$\leq \int dr \int d\theta | B(r, \theta) | | R(r, \theta) | | a(x_n) e^{-j\omega_0 t_n(r, \theta)} - a(x_k) e^{-j\omega_0 t_k(r, \theta)} e^{j\phi_e} | \quad (\text{A.11})$$

$$\quad (\text{A.12})$$

Using paraxial approximation, the flight time can be written as $t_i(r, \theta) = (r - x_i \sin \theta)/c$. Also, assume that the contributions of scatterers in the range of $(r_0 \pm \Delta r)$ are effective on the received signals. Further, assume that the transmitted beam is sufficiently narrow and constant over $(r_0 \pm \Delta r)$ so that $B(r, \theta) = \delta(\theta - \theta_0)$. Then, we can write expression as

$$\epsilon \leq \int_{r_0 - \Delta r}^{r_0 + \Delta r} | R(r, \theta_0) | dr | a(x_n) e^{j\omega_0 x_n \sin \theta_0} - a(x_k) e^{-j\omega_0 x_k \sin \theta_0} e^{j\phi_e} | \quad (\text{A.13})$$

Integral of the reflector function results in a constant, say R_0 . Hence,

$$\epsilon \leq 2R_0 \left| \sin \left\{ \frac{\omega_0}{2c} (x_n - x_k) \sin \theta_0 - \frac{1}{2} \{ \phi_a(x_n) - \phi_a(x_k) - \phi_e \} \right\} \right| \quad (\text{A.14})$$

The relative phase which makes the right side to be zero, is given by

$$\phi_e = \beta(x_n - x_k) \sin \theta_0 + \phi_a(x_n) - \phi_a(x_k) \quad (\text{A.15})$$

The first term is the steering phase for the steering angle θ_0 whereas the last two terms is the phase difference between the two channels.

Note that, in phase aberration correction, since the steering and focusing delays are known, they are subtracted from the estimated delay profile to obtain the aberration delay pattern. As a result, it is shown that error function is a direct measure for relative phase between two RF signals reflected from the random scatterers as well as from the point targets.

Appendix B

Accuracy of Time Delay Estimate

It is difficult to obtain analytical bounds for the accuracy of the time delay estimation via SAD minimization because of the non-linear nature of SAD function. In addition, these bounds may not reveal the relevant information for aberration correction performance, because of the practical limitations on accuracy, such as delay quantization. Therefore, the accuracy analysis of time delay estimation using SAD is performed, and compared to that of the correlation using the numerical simulations employing the practical limitations.

The mean and standard deviation of the time delay estimate using SAD and correlation are obtained for two band limited random (Gaussian) signals. The estimation is performed for different time delays, and repeated on uncorrelated signals to obtain the statistical results. Fig. B.1 indicates the simulation parameters, and depicts the mean and standard deviation of the time delay estimate for SAD and correlation. The figure indicates that the mean of the estimate with both schemes are zero, and the standard deviation is approximately one half of delay quantization level, $\pi/32$.

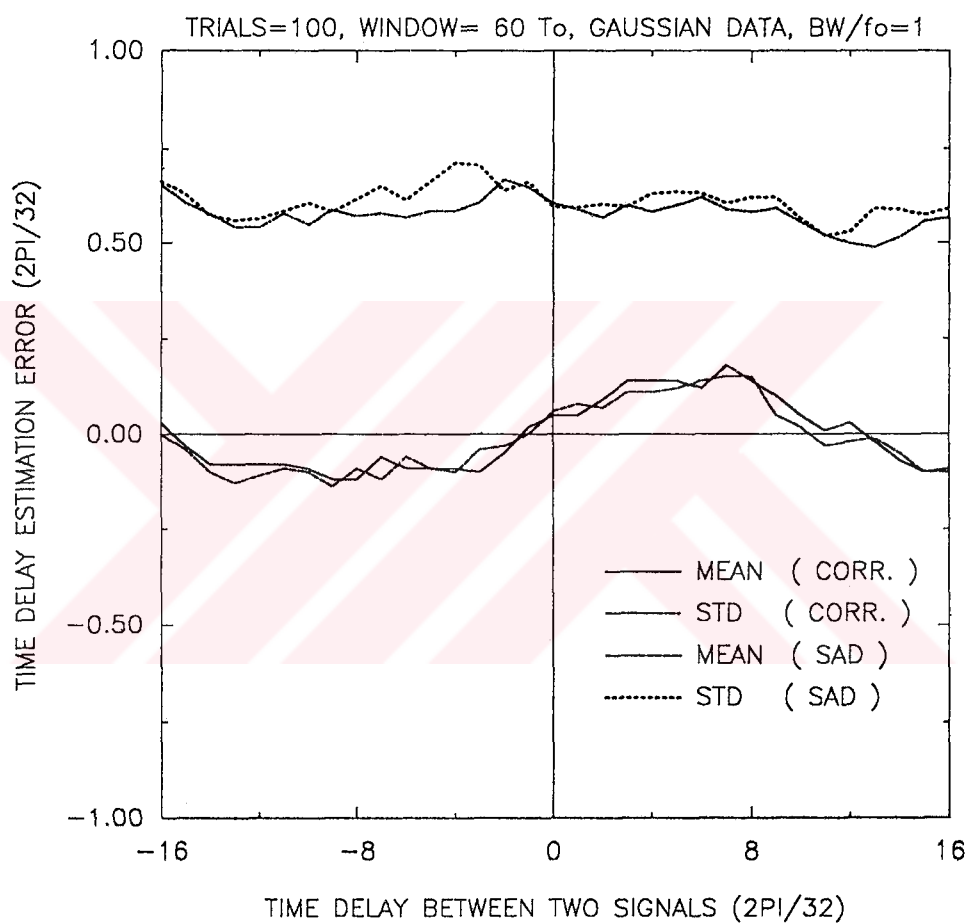


Figure B.1: Numerical simulation results showing the mean and standard deviation of time delay estimate using cross correlation and SAD.

Appendix C

Spatial Covariance Measurements

Accuracy of the estimation of relative time difference between two RF signals depends on the covariance of the two signals. The accuracy decreases as the covariance decreases. Hence, the spatial covariance of RF signals over the phased array is a critical measure for the aberration correction based on time delay estimation. According to the van Cittert-Zernike theorem applied to the pulse-echo ultrasound, the spatial covariance measured by correlation is linear across the array [100]. Time delay estimation through SAD minimization necessitates the measurement of spatial covariance across the array by employing SAD as the covariance function.

Spatial covariance measurements across the array using SAD and correlation functions are obtained for different cases such as focused, non-focused, non-aberrated, aberrated cases, and one bit wavelength. (see Fig. C.1, Fig. C.2, and Fig. C.3). These measurements are performed on the experimental non-aberrated and aberrated RF data sets previously described in Chapter 3 and Chapter 4. The covariance measurement is performed for different pairs of array elements, and hence the the difference in element numbers correspond to the spatial distance on the array. The spatial covariance measurements with different pairs but with equal differences in their element numbers are averaged. Note that the maximum/minimum covariance measured by SAD corresponds to zero/unity whereas it is unity/zero for correlation.

From Fig. C.1, Fig. C.2, and Fig. C.3, the followings observations are made.

- When the transmit and receive focusing are employed, the spatial covariance measured by the correlation is approximately linear across the array as expected from the van Cittert-Zernike theorem, whereas it is not linear for the SAD.
- The absence of the transmit and/or receive focusing critically decreases both the correlation and SAD covariance by almost the same amount. This implies that the phase estimation must be performed after receive focusing delays are employed.
- The correlation covariance for relatively small spatial distances is higher than SAD covariance.
- Presence of aberration decreases both the correlation and the SAD covariance by the same amount. Decrease in the covariance from Plate 0 to Plate 1 (RMS aberration from 0.00 Radians to 0.75 Radians) is not the same as that from Plate 1 to Plate 2 (RMS aberration from 0.75 Radians to 1.50 Radians). Hence, the decrease in the covariance is not linearly proportional with increase in the RMS aberration level.
- The reduction of the wordlength of RF samples to a single bit does not significantly reduce the SAD covariance.
- Even in the presence of large amount of aberration, it is observed that both the SAD and correlation covariance measures of the channels separated by upto 10 % of the full array aperture are acceptable for the time delay estimation.
- Both the correlation and SAD measures, even with one bit wordlength, can be used for phase correction in the presence of dead elements upto 10 % of overall elements.

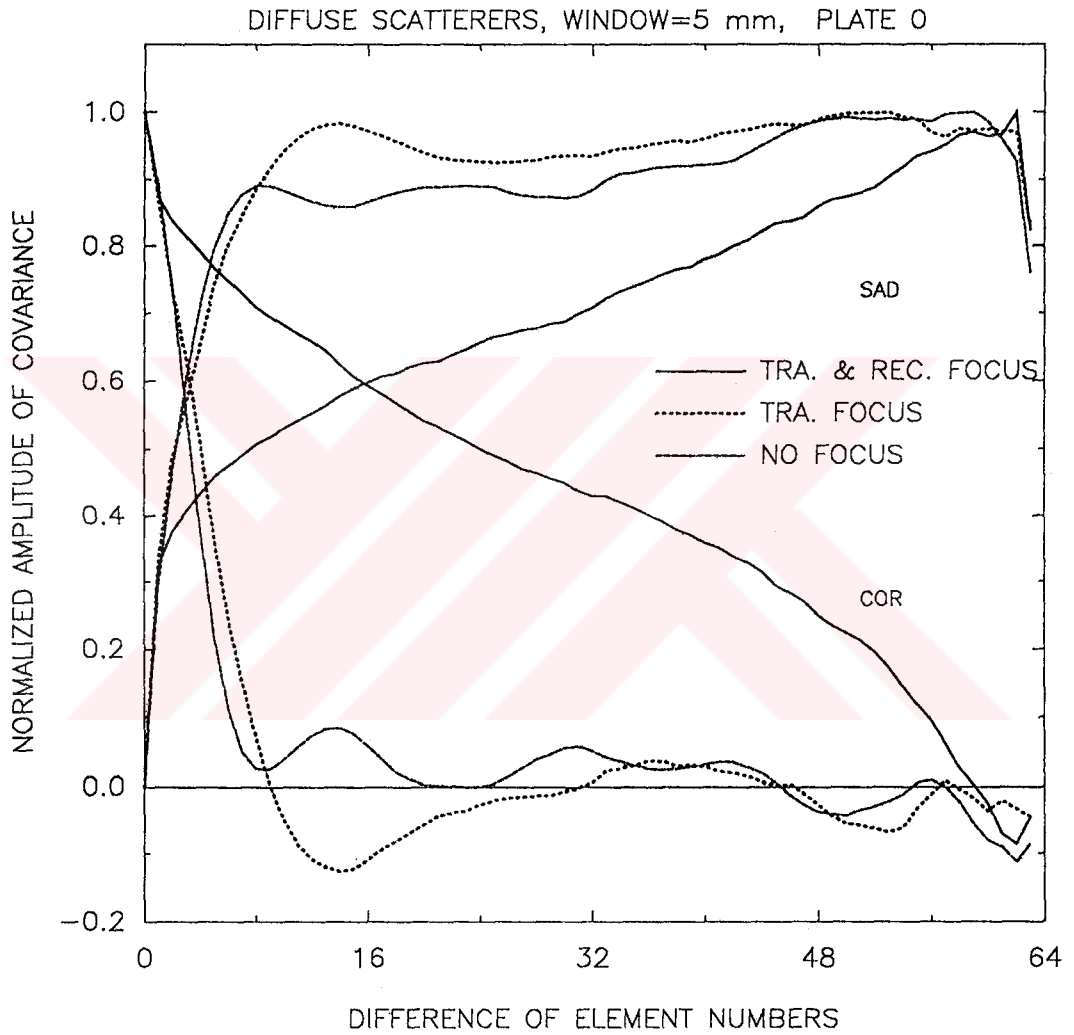


Figure C.1: Spatial covariance across the array using correlation (COR) and sum of absolute difference (SAD) for non-focused and focused cases.

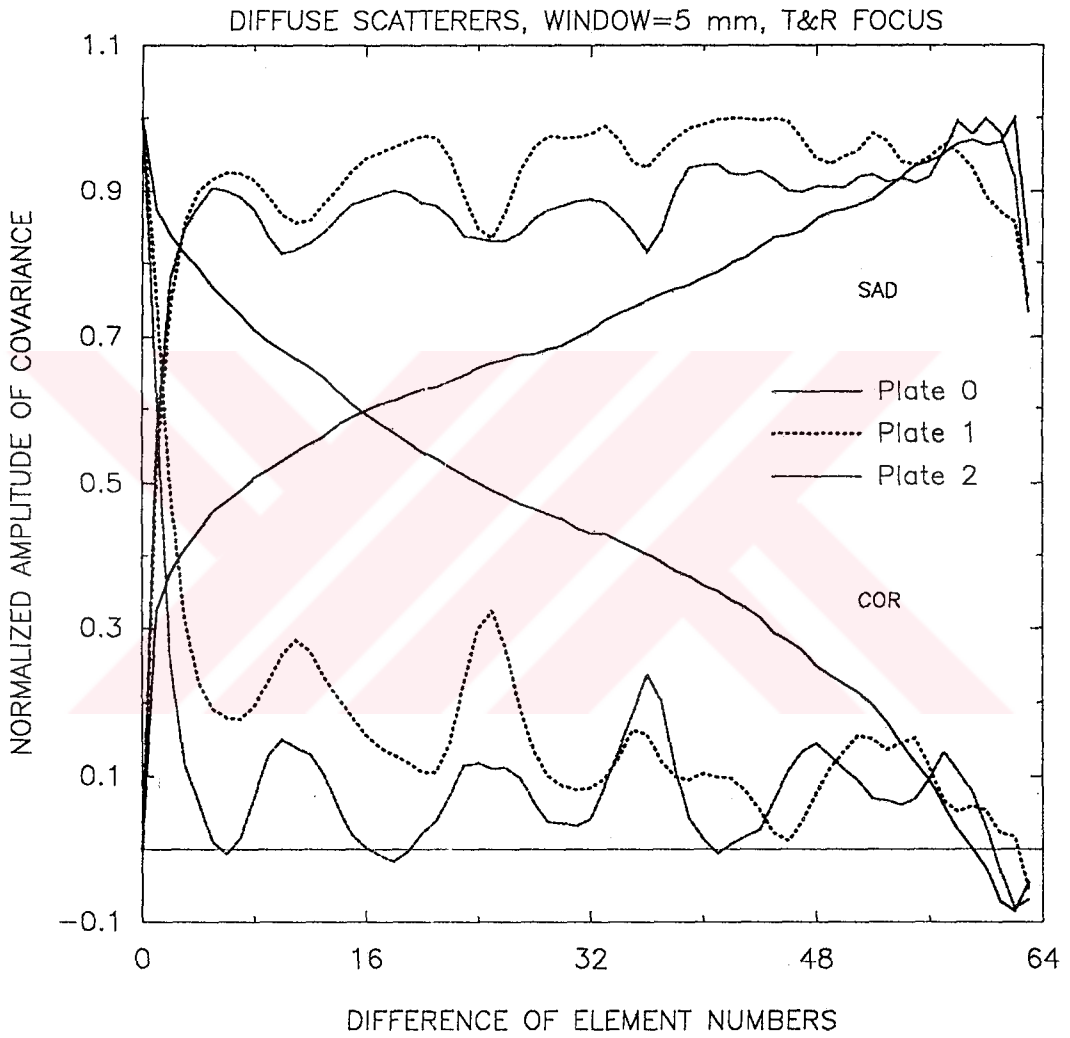


Figure C.2: Spatial covariance across the array using correlation (COR) and sum of absolute difference (SAD) for non-aberrated and aberrated data.

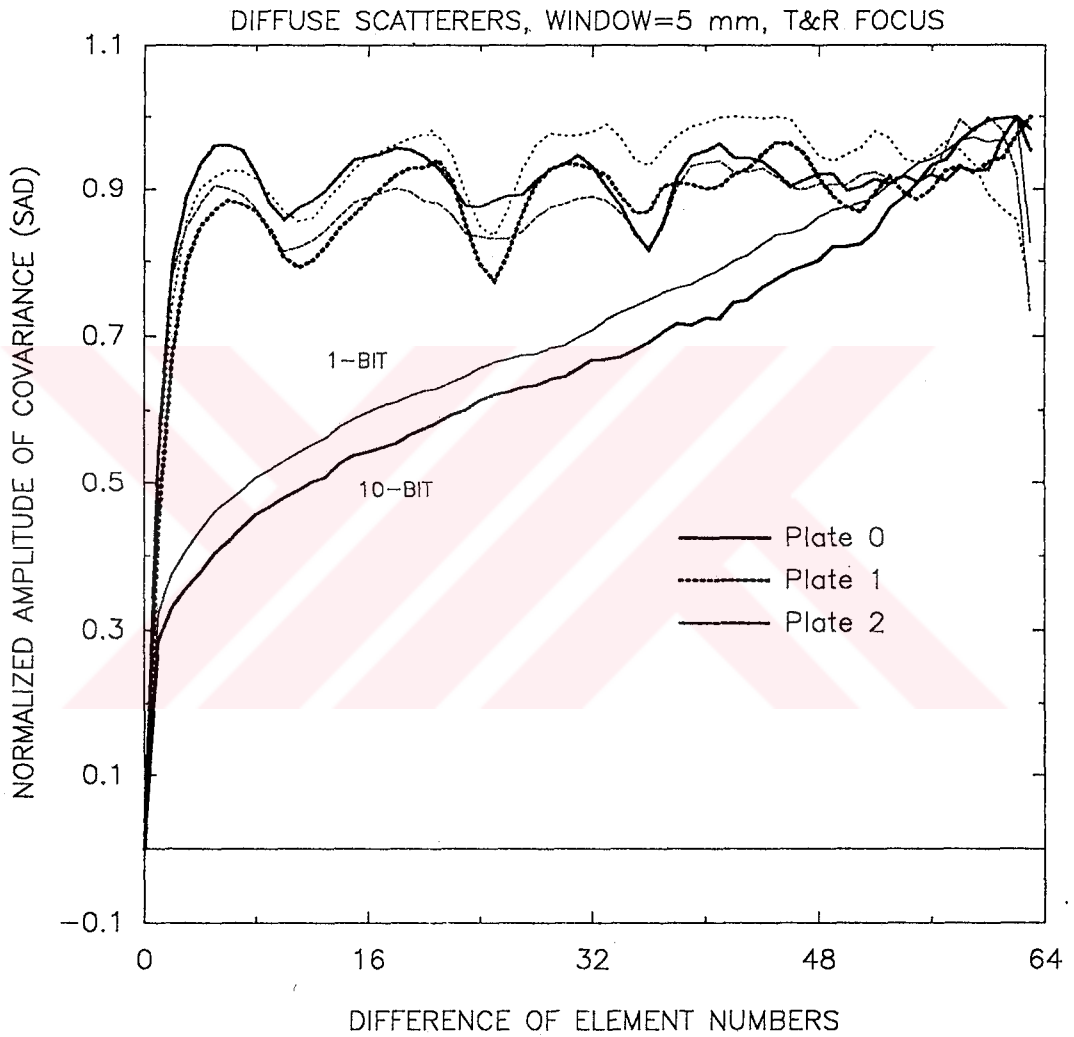


Figure C.3: Spatial covariance across the array using fullword SAD and one-bit SAD.

Appendix D

Beamforming by Phasing in RF Subbands

In the front-end hardware architecture shown in Fig. 3.1 in Chapter 3, beamforming is based on the time delay and sum operations. Beamforming by employing course time delays followed by fine phase adjustment and sum operations, have been also used [92, 23]. The course delay for each channel is quantized by the sampling period, and the phase delay accuracy is a small fraction of the sampling period. Promising feature of this approach is that the phase delays can be accurately realized by the phase rotation techniques, and the sampling rate of the ADC's can be kept at the Nyquist rate of RF signal. The phase rotation in [92] has been handled with a high efficiency by the coordinate transformation using the Coordinate Rotation Digital Computer (CORDIC) algorithm [106, 107]. The main disadvantage of this scheme is that the phase rotation introduces error because it can be adjusted correctly to only a single frequency component in the RF band, which is chosen to be the carrier frequency. The effect of this error on the array response has been studied and reported in [23]. It results in increased sidelobe level, and its elimination necessitates a sampling rate of 4 to 10 times the transducer bandwidth. This is a major limitation for phase rotation based beamforming.

The error due to phase rotation can be reduced by employing the phasing in subbands of the RF signals. This can be achieved by generating the subband signals by filtering the RF signals using narrowband filters, and perform proper phasing corresponding to the center frequency of the subband, and sum the

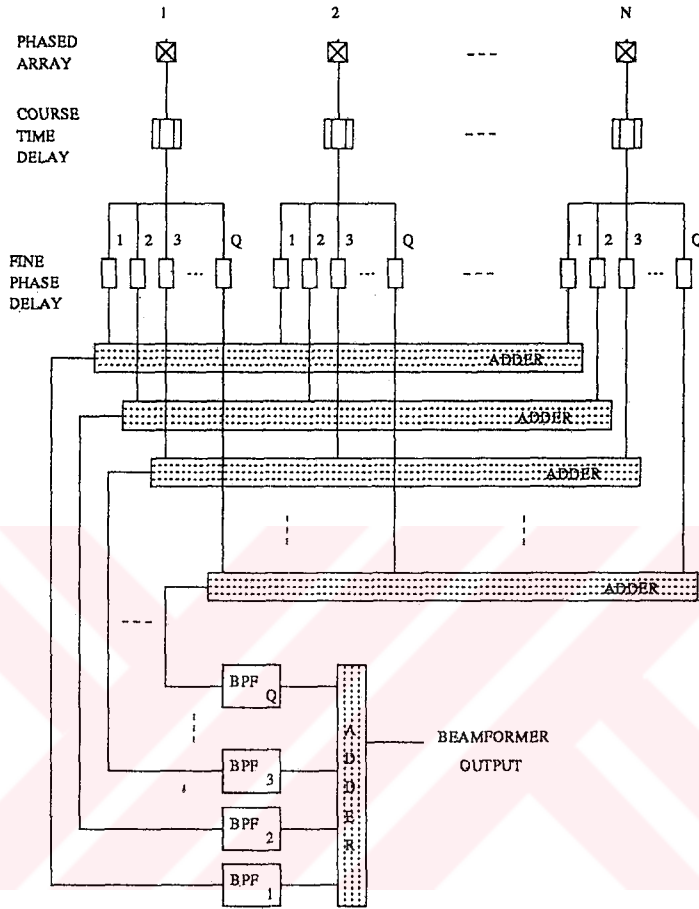


Figure D.1: Beamforming scheme employing parallel phase delay adjustment in subbands of RF signals.

results. Efficiency of this scheme can be increased further by changing the order of filtering and phasing. This modification, based on the linearity of the operations, decreases the number of the bandpass filter from $Q \times N$ to Q for an N -element array and Q subbands. A beamforming scheme based on this approach is depicted in Fig. D.1. In this scheme, RF signal in each channel is fed through parallel phase delays. Each of these phase delays corresponds to the fine time delay multiplied with the center frequency of a particular subband in the RF band. The RF signals phased for a subband are added and filtered with a bandpass filter with the passband corresponding to this subband. Finally, the bandpass filtered RF signals are added to obtain the beamformer output.

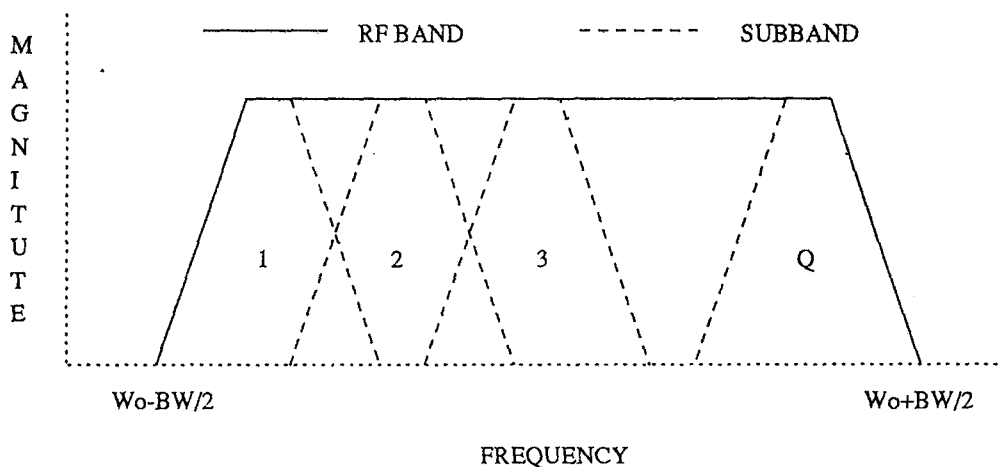


Figure D.2: RF Subbands.

Beamforming structure shown in Fig. D.1 introduces a hardware overhead due to the parallel phase delays, adders, and bandpass filters. The bandpass filters are ideally narrowband, nonoverlapping filters to cover overall RF band. The filter requirements, however, can be relaxed by overlapping the pass bands of adjacent filters as depicted in Fig. D.2. This significantly decreases the cost of filters.

Number of the subbands and the amount of overlap of passbands of filters can be properly specified through the analytical and/or experimental analysis of the scheme for the desired beamforming performance of imaging system.

Bibliography

- [1] M. G. Maginness "Methods and Terminology for diagnostic ultrasound imaging systems," *Proc. IEEE*, vol. 67, pp. 641–653, April 1979.
- [2] J. F. Havlice and J. C. Taenzer "Medical ultrasound imaging: an overview of principles and instrumentation," *Proc. IEEE*, vol. 67, pp. 620–641, April 1979.
- [3] A. Macovski "Ultrasonic imaging using arrays," *Proc. IEEE*, vol. 67, pp. 484–495, April 1979.
- [4] H. E. Karrer and A. M. Dickey "Ultrasound imaging: an overview," *Hewlett-Packard J.*, vol. 34, pp. 3–6, October 1983.
- [5] B. D. V. Veen and K. M. Buckley "Beamforming: a versatile approach to spatial filtering," *IEEE ASSP Magazine*, vol. 5, pp. 4–24, April 1988.
- [6] T. A. Shoup and J. Hart "Ultrasonic imaging systems," in *Proc. of 1988 IEEE Ultrason. Symp.*, pp. 863–871, 1988.
- [7] P. N. Keating, T. Sawatari, and G. Zilinskas "Signal Processing in acoustical imaging," *Proc. of IEEE*, vol. 67, pp. 496–509, April 1979.
- [8] M. Fatemi and A. C. Kak "Ultrasonic B-scan imaging: theory of image formation and a technique for restoration," *Ultrasonic Imaging*, vol. 2, pp. 1–47, 1980.
- [9] W. Vollmann "Resolution enhancement of ultrasonic B-scan images by deconvolution," *IEEE Sonics. Ultrason.*, vol. 29, pp. 78–83, March 1982.

- [10] C. N. Liu, M. Fatemi, and R. C. Waag "Digital processing for improvement of ultrasonic abdominal images," *IEEE Trans. Medical Imaging*, vol. 2, pp. 66-75, 1983.
- [11] J. P. Ardouin and A. N. Venetsanopoulos "Modelling and restoration of ultrasonic phased-array B-scan images," *Ultrasonic Imaging*, vol. 7, pp. 321-344, 1985.
- [12] D. Iraca, L. Landini, and L. Verrazzani "A piece-wise spatial invariant model of ultrasonic image formation," *IEEE Trans. Ultrason., Ferroelect., Freq. Contr.*, vol. 53, pp. 457-463, July 1988.
- [13] M. E. Schafer and P. A. Lewin "The influence of front-end hardware on digital ultrasonic imaging," *IEEE Trans. Sonics. Ultrason.*, vol. 31, pp. 295-306, July 1984.
- [14] M. O'Donnel "Applications of VLSI circuits to medical imaging," *Proc. IEEE*, vol. 76, pp. 1106-1114, September 1988.
- [15] A. L. Robinson and J. H. Mo "Application of microelectronics and microfabrication technology to ultrasound imaging systems," in *Proc. of 1991 IEEE Ultrason. Symp. (to be published)*, 1992.
- [16] R. N. McKnight "A mixing scheme to focus a transducer array," *Hewlett-Packard J.*, vol. 34, pp. 16-17, October 1983.
- [17] G. Manes and et. al. "Synchronous dynamic focusing for ultrasound imaging," *IEEE Trans. Ultrason. Ferroelec. Freq. Contr.*, vol. 35, pp. 14-21, January 1988.
- [18] R. A. Harris and et. al "Ultimate limits in ultrasonic image resolution," *Ultrasound in Med. and Biol.*, vol. 17, pp. 547-558, 1991.
- [19] M. J. Foster and H. T. Kung "The design of special purpose VLSI chips," *IEEE Computer*, pp. 26-40, January 1980.

- [20] P. A. Magnin, O. V. Ramm, and F. L. Thurstone "Delay quantization error in phased array images," *IEEE Sonics. Ultrason.*, vol. 28, pp. 305–310, September 1981.
- [21] D. K. Peterson and G. S. Kino "Real-time digital image reconstruction: a description of imaging hardware and an analysis of quantization errors," *IEEE Sonics. Ultrason.*, vol. 31, pp. 337–351, July 1984.
- [22] S. Holm and K. Kristoffersen "Analysis of worst-case phase quantization sidelobes in focused beamforming," *IEEE Trans. Ultrason. Ferroelec. Freq. Contr.*, vol. 39, pp. 593–599, September 1992.
- [23] B. D. Steinberg "Digital beamforming in ultrasound," *IEEE Trans. Ultrason. Ferroelec. Freq. Contr.*, vol. 39, pp. 716–721, November 1992.
- [24] Y. C. Lim and S. R. Parker "FIR filter designed over a discrete powers-of-two coefficient space," *IEEE Trans. Acoust., Speech, Signal Processing*, vol. 31, pp. 583–590, June 1983.
- [25] J. Ophir and N. F. Maklad "Digital scan converters in diagnostic ultrasound imaging," *Proc. IEEE*, vol. 67, pp. 654–664, April 1979.
- [26] M. O'Donnell and S. W. Flax "Phase aberration measurements in medical ultrasound: human studies," *Ultrasonic Imaging*, vol. 10, pp. 1–11, 1988.
- [27] G. E. Trahey and et. al. "In vivo measurements of ultrasonic beam distortion in the breast," *Ultrasonic Imaging*, vol. 13, pp. 71–90, 1991.
- [28] L. I. Halberg and E. Thiele "Extraction of blood flow information using doppler-shifted ultrasound," *Hewlett-Packard J.*, pp. 35–40, June 1986.
- [29] F. J. Fry "Biological effects of ultrasound a review," *Proc. of IEEE*, vol. 67, pp. 604–619, April 1979.
- [30] O. V. Ramm and S. W. Smith "Beam steering with linear arrays," *IEEE Trans. Biomed. Eng.*, vol. 30, pp. 438–452, August 1983.

- [31] R. A. Snyder and R. J. Conrad "Ultrasound image quality," *Hewlett-Packard J.*, vol. 34, pp. 34–38, October 1983.
- [32] C. R. Hill, J. C. Bamber, D. C. Crawford, H. J. Lowe, and S. Webb "What might echography learn from image science?," *Ultrasound in Med. and Biol.*, vol. 17, pp. 559–575, 1991.
- [33] J. H. Kim, T. K. Song, and S. B. Park "Pipelined sampled-delay focusing in ultrasound imaging systems," *Ultrasonic Imaging*, vol. 9, pp. 75–91, 1987.
- [34] R. M. Lutolf, A. Vieli, and S. Basler "Ultrasonic phased-array scanner with digital echo synthesis for Doppler echocardiography," *IEEE Trans. Ultrason. Ferroelect. Freq. Contr.*, vol. 36, pp. 494–506, September 1989.
- [35] R. G. Pridham and R. A. Mucci "A novel approach to digital beamforming," *J. Acoust. Soc. Amer.*, vol. 63, pp. 425–434, February 1978.
- [36] R. G. Pridham and R. A. Mucci "Digital interpolation beamforming for low-pass and bandpass signals," *Proc. IEEE*, vol. 67, pp. 904–919, April 1979.
- [37] J. E. Powers and et. al. "Ultrasound phased array delay lines based on quadrature sampling techniques," *IEEE Trans. Sonics. Ultrason.*, vol. 27, pp. 287–294, November 1980.
- [38] S. M. Gehlbach and R. E. Alvarez "Digital ultrasound imaging techniques using vector sampling and raster line reconstruction," *Ultrasonic Imaging*, vol. 3, pp. 83–107, 1981.
- [39] S. Leavitt, B. F. Hunt, and H. G. Larsen "A scan conversion algorithm for displaying ultrasound images," *Hewlett-Packard J.*, vol. 34, pp. 30–34, October 1983.
- [40] M. Karaman, A. Atalar, and H. Köymen "Optimization of dynamic receive focusing in ultrasound imaging," in H. Ermert and H. P. Harjes, eds., *Acoustical Imaging*, pp. 225–229. Plenum Press, New York, 1992. vol. 19.

- [41] M. Karaman, A. Atalar, and H. Köymen "Radyal ve raster noktalara odaklamalı ultrasonik sektör tarama yöntemlerinin karşılaştırılması," in *Bilkon91*, pp. 245–248, 1991.
- [42] J. C. Bamber and R. J. Dickinson "Ultrasonic B-scanning: a computer simulation," *Phys. Med. Biol.*, vol. 25, pp. 463–479, 1980.
- [43] R. Kuc and H. Miwa "A computer model for simulating reflected ultrasound signals," *J. Acoust. Soc. Amer.*, vol. 80, pp. 951–954, 1986.
- [44] G.S. Kino. *Acoustic Waves: Devices, Imaging and Analog Signal Processing*. Prentice-Hall, Englewood Cliffs, 1987.
- [45] S. W. Flax and M. O'Donnell "Phase-aberration correction using signals from point reflectors and diffuse scatterers: basic principles," *IEEE Trans. Ultrason. Ferroelec. Freq. Contr.*, vol. 35, pp. 758–767, November 1988.
- [46] M. O'Donnell and S. W. Flax "Phase-aberration correction using signals from point reflectors and diffuse scatterers: experimental results," *IEEE Trans. Ultrason. Ferroelec. Freq. Contr.*, vol. 35, pp. 768–774, November 1988.
- [47] J. P. Stonestorm and W. A. Anderson "Custom NMOS chip for medical ultrasound," *VLSI Design*, pp. 44–49, May 1982.
- [48] T. H. Song and S. B. Park "A new digital phased array system for dynamic focusing and steering with reduced sampling rate," *Ultrasonic Imaging*, vol. 12, pp. 1–16, 1990.
- [49] M. Karaman, A. Atalar, and C. Aykanat "A front-end digital hardware architecture for real-time ultrasound imaging," in E. Arkan, ed., *Communication, Control, and Signal Processing*, pp. 1612–1618. Elsevier Science Publishers, Ankara, 1990.

- [50] M. Karaman, E. Kolağasıoğlu, and A. Atalar "A VLSI receive beamformer for digital ultrasound imaging," in *Proc. of ICASSP'92*, pp. V-657-660, 1992.
- [51] M. Karaman, A. Atalar, and H. Köymen "Ultrasonik görüntüleme de alışı odaklamasının eniyilenmesi," in *Elektrik Müh. IV. Ulusal Kongresi*, pp. 586-589, 1991.
- [52] M. Karaman, A. Atalar, and H. Köymen "VLSI circuits for adaptive digital beamforming in ultrasound imaging," *Submitted to IEEE Trans. Medical Imaging*.
- [53] C. N. Dorny "A self-survey technique for self-cohering of antenna systems," *IEEE Trans. Antennas. Propagat.*, vol. 26, pp. 877-881, November 1978.
- [54] M. Hirama, O. Ikeda, and T. Sato "Adaptive ultrasonic array imaging system through an inhomogeneous layer," *J. Acoust. Soc. Amer.*, vol. 71, pp. 100-109, January 1982.
- [55] M. Hirama and T. Sato "Imaging through an inhomogeneous layer by least-mean-square error fitting," *J. Acoust. Soc. Amer.*, vol. 75, pp. 1142-1147, April 1984.
- [56] S. W. Smith, G. E. Trahey, and O. T. von Ramm "Phased array ultrasound imaging through planar tissue layers," *Ultrasound in Med. and Biol.*, vol. 12, pp. 229-243, March 1986.
- [57] M. O'Donnell and W. E. Engeler "Real-time phase aberration correction system for medical ultrasound imaging," in *Proc. of 1990 Annual Int. Conf. of IEEE EMBS*, pp. 278-280, 1991.
- [58] M. O'Donnell and W. E. Engeler "Correlation-based aberration correction in the presence of inoperable elements," *IEEE Trans. Ultrason. Ferroelec. Freq. Contr.*, vol. 39, pp. 700-707, November 1992.

- [59] L. Nock, G. E. Trahey, and S. W. Smith "Phase aberration correction in medical ultrasound using speckle brightness as a quality factor," *J. Acoust. Soc. Amer.*, vol. 85, pp. 1819–1833, May 1989.
- [60] G. E. Trahey and et. al. "Experimental results with a real-time adaptive ultrasonic imaging system through distorting media," *IEEE Trans. Ultrason. Ferroelec. Freq. Contr.*, vol. 37, pp. 418–427, September 1990.
- [61] D. Zhao and G. E. Trahey "Comparisons of image quality factors for phase aberration correction with diffuse and point targets," *IEEE Trans. Ultrason. Ferroelec. Freq. Contr.*, vol. 38, pp. 125–132, March 1991.
- [62] F. Wu and et. al. "Optimal focusing through aberrating media: a comparison between time reversal mirror and time delay correction techniques," in *Proc. of 1991 IEEE Ultrason. Symp.*, pp. 1195–1199, 1991.
- [63] M. Fink "Time reversal of ultrasonic fields - Part I: basic principles," *IEEE Trans. Ultrason. Ferroelec. Freq. Contr.*, vol. 39, pp. 555–566, September 1992.
- [64] C. R. Giuliano "Applications of optical phase conjugation," *Physics Today*, pp. 27–35, April 1981.
- [65] G. E. Trahey and P. D. Freiburger "An evaluation of transducer design and algorithm performance for two dimensional phase aberration correction," in *Proc. of 1991 IEEE Ultrason. Symp.*, pp. 1181–1187, 1991.
- [66] M. O'Donnell and P. C. Li "Aberration correction on a two-dimensional anisotropic phased array," in *Proc. of 1991 IEEE Ultrason. Symp.*, pp. 1189–1193, 1991.
- [67] R. Kanda and et. al. "An investigation of wavefront distortion correction: correction using averaged phase information and the effect of correction one and two dimensions," in *Proc. of 1991 IEEE Ultrason. Symp.*, pp. 1201–1206, 1991.

- [68] D. M. Etter and S. D. Stearns "Adaptive estimation of time delays in sampled data systems," *IEEE Trans. Acoust. Speech, Signal Processing*, vol. 29, pp. 582-587, June 1981.
- [69] C. H. Knapp and G. C. Carter "The generalized correlation method for estimation of time delay," *IEEE Trans. Acoust. Speech, Signal Processing*, vol. 24, pp. 320-327, August 1976.
- [70] K. Scarbrough, N. Ahmed, and G. C. Carter "On the simulation of a class of time delay estimation algorithms," *IEEE Trans. Acoust. Speech, Signal Processing*, vol. 29, pp. 534-539, June 1981.
- [71] L. E. Franks "Carrier and bit synchronization in data communication- a tutorial review," *IEEE Trans. Commun.*, vol. 28, pp. 1107-1120, August 1980.
- [72] D. I. Barnea and H. F. Silverman "A class of algorithms for fast digital image registration," *IEEE Trans. Comput.*, vol. 21, pp. 179-186, February 1972.
- [73] M. Ross and et. al. "Average magnitude difference function pitch extractor," *IEEE Trans. Acoust. Speech, Signal Process.*, vol. 22, October 1974.
- [74] L. N. Bohs and G. E. Trahey "A novel method for angle independent ultrasonic imaging of blood flow and tissue motion," *IEEE Trans. Biomed. Eng.*, vol. 38, pp. 280-286, March 1991.
- [75] E. J. Coyle "Rank order operators and the mean absolute error criterion," *IEEE Trans. Acoust. Speech, Signal Processing*, vol. 36, pp. 63-76, January 1988.
- [76] P. Maragos "Morphological correlation and mean absolute error criteria," in *Proc. of ICASSP'89*, pp. 1568-1571, 1989.

- [77] M. Karaman, A. Atalar, and H. Köymen “Adaptive digital beamforming for real-time phased array ultrasound imaging,” in *Proc. of 1991 IEEE Ultrason. Symp.*, pp. 1207–1210, 1991.
- [78] B. D. Steinberg and E. Yadin “Effect of multipath and scattering on array gain of large adaptive beam forming array,” *IEEE Trans. Antennas. Propagat.*, vol. 33, pp. 481–487, May 1985.
- [79] Jr. B. F. Logan “Information in the zero crossings of bandpass signals,” *Bell System Technical J.*, vol. 56, pp. 487–510, April 1977.
- [80] I. F. Blake and W. C. Lindsey “Level-crossing problems for random process,” *IEEE Trans. Inform. Theory*, vol. 19, pp. 295–315, May 1973.
- [81] M. Karaman, A. Atalar, H. Köymen, and M. O’Donnell “Experimental analysis of a computationally efficient phase aberration correction technique,” in *Proc. of 1992 IEEE Ultrason. Symp. (to be published)*, 1992.
- [82] M. Karaman, A. Atalar, H. Köymen, and M. O’Donnell “A phase aberration correction method for ultrasound imaging,” *Submitted to IEEE Trans. Ultrason., Ferroelect., Freq. Contr.*
- [83] C. Mead and L. Conway. *Introduction to VLSI Systems*. Addison-Wesley, Reading MA, 1980.
- [84] H. T. Kung “Why systolic architectures?,” *IEEE Computer*, pp. 37–46, January 1982.
- [85] D. L. Knuth. *The Art of Computer Programming-Searching and Sorting*. Addison-Wesley, Reading MA, 1973.
- [86] M. Karaman, L. Onural, and A. Atalar “Design and implementation of a general-purpose median filter unit in CMOS VLSI,” *J. Solid-State Cir.*, vol. 25, pp. 505–5113, April 1990.

- [87] R. D. Davis "The case for CMOS," *IEEE Spectrum*, pp. 26–32, October 1983.
- [88] N. Weste and K. Eshraghian. *Principles of CMOS VLSI Design*. Addison-Wesley, Reading MA, 1985.
- [89] *Berkeley CAD Tools User's Manual*. University of California at Berkeley, 1986.
- [90] *VLSI Tools Reference Manual*. University of Washington, 1987.
- [91] J. A. Abraham and W. K. Fuchs "Fault and error models for VLSI," *Proc. IEEE*, pp. 639–654, May 1986.
- [92] M. O'Donnel and et. al. "Real-time phased-array imaging using digital beam forming and autonomous channel control," in *Proc. of 1990 IEEE Ultrason. Symp.*, pp. 1499–1502, 1990.
- [93] M. O'Donnel "Private communication,". 1991.
- [94] D. H. Turnbull and F. S. Foster "Beam steering with pulsed two-dimensional transducer arrays," *IEEE Trans. Ultrason., Ferroelect., Freq. Contr.*, vol. 38, pp. 320–333, July 1991.
- [95] S. W. Smith, H. Puly, and O. von Ramm "High-speed ultrasound volumetric imaging systems: - part I: transducer design and beam steering," *IEEE Trans. Ultrason., Ferroelect., Freq. Contr.*, vol. 38, pp. 100–108, March 1991.
- [96] O. von Ramm, S. W. Smith, and H. Puly "High-speed ultrasound volumetric imaging systems: - part II: parallel processing and image display," *IEEE Trans. Ultrason., Ferroelect., Freq. Contr.*, vol. 38, pp. 109–115, March 1991.
- [97] H. W. Durgin, P. D. Freiburger, G. E. Trahey, and D. C. Sullivan "Large aperture phase error measurements and effects," in *Proc. of 1991 IEEE Ultrason. Symp. (to be published)*, 1992.

- [98] L. Nock and G. E. Trahey "Synthetic receive aperture imaging with phase correction for motion and for tissue inhomogeneties - Part I: basic principles," *IEEE Trans. Ultrason. Ferroelec. Freq. Contr.*, vol. 39, pp. 489-495, July 1992.
- [99] P. C. Li, S. F. Flax, E. S. Ebbini, and M. O'Donnell "Object dependent compansation of missing array elemnts," in *Proc. of 1991 IEEE Ultrason. Symp. (to be published)*, 1992.
- [100] R. Mallart and M. Fink "The van Cittert-Zernike theorem in pulse-echo measurements," *J. Acoust. Soc. Amer.*, vol. 90, pp. 2718-2727, 1991.
- [101] C. B. Burckhardt "Speckle in ultrasound B-mode scans," *IEEE Trans. Sonic. Ultrason.*, vol. 25, pp. 1-6, January 1978.
- [102] R. F. Wagner, M. F. Insana, and D. G. Brown "Statistical properties of radio-frequency and envelope-detected signals with applications to medical ultrasound," *J. Opt. Soc. Am.: A*, vol. 4, pp. 910-922, May 1987.
- [103] R. F. Wagner, S. W. Smith, J. M. Sandrik, and H. Lopez "Statistics of speckle in ultrasound B-scans," *IEEE Trans. Sonic. Ultrason.*, vol. 30, pp. 156-163, May 1983.
- [104] T. Loupas, W. N. Mcdicken, and P. L. Allan "An adaptive weighted median filter for speckle suppression in medical ultrasonic images," *IEEE Trans. Circuit and Systems*, vol. 36, pp. 129-135, January 1989.
- [105] R. Suoranta "Novel ultrasonic beamforming method based on nonlinear filtering," in *Proc. of 1991 IEEE Ultrason. Symp. (to be published)*, 1992.
- [106] Y. H. Hu "CORDIC-Based VLSI architectures for digital signal processing," *IEEE Signal Processing Magazine*, vol. 9, pp. 16-35, July 1992.

- [107] D. Timmermann, H. Hahn, B. J. Hosticka, and G. Schmit "A programmable CORDIC chip for digital signal processing applications," *J. Solid-State Cir.*, vol. 26, pp. 1317-1321, September 1991.



Vita

Mustafa Karaman was born in Balıkesir, Turkey, in 1964. He received B. Sc. degree from Middle East Technical University, Ankara, Turkey, and M. Sc. degree from Bilkent University, Ankara, Turkey, in 1986 and 1988, respectively, both in Electrical and Electronics Engineering. His research interests include VLSI signal processing and medical ultrasound imaging.

**T.C. YÜKSEKÖĞRETİM KURULU
DOKÜMANTASYON MERKEZİ**